

Lane-Level Localization and Mapping in GNSS-Challenged Environments by Fusing Lidar Data and Cellular Pseudoranges

Mahdi Maaref, Joe Khalife, *Student Member, IEEE*, and Zaher M. Kassas, *Senior Member, IEEE*

Abstract—A method for achieving lane-level localization in global navigation satellite system (GNSS)-challenged environments is presented. The proposed method uses the pseudoranges drawn from unknown ambient cellular towers as an exclusive aiding source for a vehicle-mounted light detection and ranging (lidar) sensor. The following scenario is considered. A vehicle aiding its lidar with GNSS signals enters an environment where these signals become unusable. The vehicle is equipped with a receiver capable of producing pseudoranges to unknown cellular towers in its environment. These pseudoranges are fused through an extended Kalman filter (EKF) to aid the lidar odometry, while estimating the vehicle’s own state (three-dimensional position and orientation) simultaneously with the position of the cellular towers and the difference between the receiver’s and cellular towers’ clock error states (bias and drift). The proposed method is computationally efficient and is demonstrated to achieve lane-level accuracy in different environments. Simulation and experimental results with the proposed method are presented illustrating a close match between the vehicle’s true trajectory and that estimated using the cellular-aided lidar odometry over a 1 km trajectory. A 60% reduction in localization error is obtained over the lidar odometry-only approach.

Index Terms—Signals of opportunity, Cellular, Lidar, SLAM

I. INTRODUCTION

LIIGHT detection and ranging (lidar) sensors are becoming prevalent in advanced driver-assistance systems (ADAS) and ground vehicles [1]–[3]. ADAS typically rely on global navigation satellite systems (GNSS) and inertial measurement units (IMUs) for navigation [4]–[6] and employ lidar sensors to sense the surrounding environment. In addition to being effective for environment mapping, lidar sensors are also effective for improving the vehicle localization accuracy due to their wide horizontal field of view, long range, and accurate measurements [7]–[9]. Recently, considerable attention has been devoted to odometry measurements by solving for the relative pose between point clouds captured by the lidar sensor [8], [10], [11].

While lidar measurements provide an accurate short-term odometry and mapping solution, one cannot rely on these measurements as a standalone, accurate solution for long-term navigation. This is due to two shortcomings. First, if

This work was supported in part by the National Science Foundation (NSF) under Grant 1566240 and in part by the Office of Naval Research (ONR) under Grant N00014-16-1-2809.

M. Maaref, J. Khalife, and Z. M. Kassas are with the Department of Electrical and Computer Engineering, The University of California, Riverside. Address: 900 University Ave., 319 Winston Chung Hall, Riverside, CA 92521, USA (email: mmaaref@ucr.edu, joe.khalife@email.ucr.edu, and zkassas@ieee.org).

the lidar sensor is continuously moving, range measurements will be received at different times, leading to distortion in the captured point clouds, which in turn degrades the navigation solution [12]. Second, since lidars are dead-reckoning (DR)-type sensors, they suffer from accumulated pose estimation error over time [13]. Thus, in long-term driving, a lidar sensor may become unreliable and an aiding source is needed to correct the drift and improve the navigation solution.

Several sensor fusion approaches have been developed to address the shortcomings of using lidar for navigation. A vision-based relative localization approach that fuses RGB-depth camera and lidar was proposed in [14]. This approach utilized an adaptive color-based particle filter and an interacting multiple mode estimator to produce two-dimensional (2-D) position estimates. A framework to augment visual odometry with lidar measurement was developed in [15]. In this framework the depth information extracted from lidar measurements is utilized as a bundle adjustment that refines the camera motion estimates in a batch optimization.

While these approaches reduce the lidar’s point cloud distortion and could precisely detect visual features, the accuracy of visual cameras deteriorates in poor lighting conditions and the methods are not useful in environments lacking sufficient structured features. Alternative sensors to the aforementioned vision-type sensors have also been studied. In [16], a framework was presented to improve three-dimensional (3-D) vehicle position estimation by fusing data from a 2-D lidar and an inertial navigation system (INS). A closed-form formula was derived to predict the line measurement in the lidar’s frame with which an extended Kalman filter (EKF) was employed to fuse the lidar and INS data.

A common approach to correct for the drift in the lidar’s navigation solution is to fuse lidar data and GNSS signals. An efficient construction of urban scenes from lidar data, which fuses the lidar point cloud and differential global positioning system (GPS) measurements was developed in [17]. The framework used a lidar sensor and a differential GPS receiver whose internal clock has been synchronized. The lidar translation vector was calculated from the GPS solution and the 3-D rotation was computed by matching planes extracted from consecutive lidar point clouds.

While GNSS provides an accurate position estimate with respect to a global frame, its signals are severely attenuated in deep urban canyons, making them unreliable to aid the lidar’s navigation solution [18]. Current trends to overcome GNSS drawbacks aim at exploiting ambient signals of opportunity

(SOPs), such as digital television, cellular signals, and AM/FM radio signals [19]–[23]. SOPs are abundant in urban canyons and are free to use. Recent work has demonstrated how SOPs could be exploited to produce a navigation solution in a standalone fashion [24], [25], to aid an INS [26]–[28], and to improve the accuracy of the GNSS navigation solution [29], [30].

Among the different types of SOPs, cellular signals are particularly attractive due to several reasons: (1) cellular towers are arranged in a favorable geometric configuration, which yields a navigation solution with low dilution of precision factors, (2) cellular signals are received at significantly higher carrier-to-noise ratio than GNSS signals (15–25 dBs higher), and (3) cellular signals' bandwidth is comparable to GPS C/A signals and recent cellular generations, specifically long-term evolution (LTE), have a bandwidth up to twenty times higher than that of GPS, which yields better suppression of multipath effects [31].

This paper considers the following practical problem. A vehicle is equipped with a GNSS receiver, a lidar sensor, and a receiver capable of producing pseudoranges to multiple unknown cellular towers. The vehicle uses GNSS signals for navigation; however, GNSS signals may become unusable along the vehicle's trajectory, e.g., in deep urban canyons. In the absence of GNSS signals, DR-type sensors (e.g., IMUs or vision sensors) can be used to improve the navigation solution. However, the navigation solution errors of DR sensors accumulated over time due to integrating noisy measurements. One may use high quality IMUs; however, the cost of an IMU increases exponentially with its quality. Moreover, while the accuracy of visual odometry improves when more features are processed, this comes at significant increase in computational burden. Therefore, achieving a good navigation performance with such sensors is significantly costly, financially and computationally.

An alternative solution to the aforementioned problem is to exploit SOPs for navigation, which are free to use and are available in situations where GNSS signals are inaccessible or unreliable. This paper takes this approach and specifically considers cellular LTE signals. The proposed framework operates in two modes. First, when GNSS signals are available, a specialized cellular receiver makes pseudorange measurements to nearby cellular towers to map these transmitters (i.e., estimate the towers' position and the difference between the receiver's and cellular transmitters' clock bias and drift). Second, when GNSS signals become unusable, the pseudoranges drawn from the mapped cellular transmitters are used exclusively as an aiding source to correct the error due to lidar odometry. To tackle these problems, an EKF-based framework is adopted that operates in a mapping mode when GNSS signals are available and in a radio simultaneous localization and mapping (SLAM) mode when GNSS signals are unusable. It is worth noting that while this paper focuses on cellular signals, the developed techniques are applicable to pseudorange measurements made to any SOP type.

Fusing lidar data and cellular signals was first introduced by [32], where an iterative closest point (ICP) algorithm was used to solve for the relative pose between lidar scans. The

framework only used 0.5% of the nearly 90,000 3-D points in every laser scans, achieving a 3-D position root mean-squared error (RMSE) of 29.6 m and a 2-D RMSE of 9.61 m, over a 1 km trajectory using three cellular code-division multiple access (CDMA) towers. The framework assumed the position of the cellular towers to be *fully known*.

The contributions of this paper are as follows. First, a precise and computationally efficient approach for extracting lidar odometry measurements is proposed. This method uses a fast and robust feature extraction technique from lidar point clouds. The proposed approach also estimates the covariance of the relative pose estimation error using a maximum likelihood estimator. The calculated covariance is used in the EKF to propagate the six-degrees of freedom (6DOF) pose estimation error covariance.

Second, the navigation problem in [32] is extended to environments in which the position of the cellular towers are *unknown*. To this end, a radio SLAM approach is adapted. It is worth mentioning that the receiver's as well as cellular transmitters' clock error states (bias and drift) are dynamic and stochastic and must be continuously estimated [33]. Therefore, in contrast to the traditional robotic SLAM problem whose environmental map [34] consists of static states (e.g., landmarks, posts, trees, etc.), the radio SLAM problem is more complex due to the dynamic and stochastic nature of the radio map. An EKF-based framework for fusing lidar odometry measurements and SOP pseudoranges is developed. This framework simultaneously localizes the vehicle-mounted receiver and maps the cellular transmitters' environment.

Third, the performance of the obtained model is analyzed through two sets of experimental tests. In the first set, lidar and GPS data from the KITTI data sets [35] are used and pseudoranges to cellular towers are simulated. In the second set, data is collected with a car equipped with a lidar sensor, a GPS-aided INS, and a cellular LTE receiver that produced pseudoranges to nearby unknown LTE towers. It is worth mentioning that in the second set of experiments, the LTE towers were obstructed and far from the vehicle (more than 1.7 km), reducing the portions of the trajectory where the vehicle-mounted receiver had line-of-sight (LOS) to the LTE towers. Experimental results compare the trajectory estimates corresponding to a lidar odometry-only navigation solution with that of the proposed cellular-aided framework. The results from both experimental sets show that the proposed framework reduces the position RMSE of the lidar odometry-only estimate by at least 60%.

It is worth noting that the proposed framework produces a navigation solution without GNSS signals or other navigation sensors (e.g., IMU) by fusing lidar data with pseudoranges from ambient SOPs in the environment. Note that an IMU will also experience drift in the absence of GNSS signals. This paper shows how cellular pseudoranges can be used as an aiding source in a global frame in the absence of GNSS signals. Nevertheless, if the vehicle is equipped with other navigation sensors, adding pseudoranges from cellular towers via the framework discussed in this paper can still improve the navigation solution.

The remainder of this paper is organized as follows. Section

II describes the models for the vehicle kinematics, cellular transmitters dynamics, lidar measurements, and cellular pseudorange measurements. Section III discusses a novel method for feature extraction and a registration method for lidar odometry. Section IV proposes an EKF-based framework for fusing lidar odometry and cellular pseudoranges in both mapping and SLAM modes. Sections V and VI provide simulation and experimental results, respectively. Concluding remarks are given in Section VII.

II. MODEL DESCRIPTION

This section presents the dynamics of the cellular tower transmitters, the vehicle's kinematics models, as well as the measurement model of the lidar and vehicle-mounted receiver.

A. SOP Dynamics Model

The navigation environment is assumed to comprise N_s cellular towers, denoted $[S_i]_{i=1}^{N_s}$. Each tower is assumed to be spatially-stationary and its state vector consists of its 3-D position states as well as the difference between its clock bias and drift with clock bias and drift of the vehicle-mounted receiver. Hence, the state of the n -th cellular tower is given by

$$\mathbf{x}_{s_n} = \left[\mathbf{r}_{s_n}^\top, \Delta\mathbf{x}_{\text{clk},s_n}^\top \right]^\top,$$

where $\mathbf{r}_{s_n} = [x_{s_n}, y_{s_n}, z_{s_n}]^\top$ is the 3-D position vector of the n -th cellular tower and

$$\Delta\mathbf{x}_{\text{clk},s_n} \triangleq \left[c\Delta\delta t_n, c\Delta\dot{\delta}t_n \right]^\top, \quad (1)$$

where c is the speed of light, $\Delta\delta t_n$ is the difference between the n -th tower's clock bias and the receiver's clock bias, and $\Delta\dot{\delta}t_n$ is the difference between the n -th tower's clock drift and the receiver's clock drift. The dynamics of the augmented vector $\Delta\mathbf{x}_{\text{clk}} \triangleq \left[\Delta\mathbf{x}_{\text{clk},s_1}^\top, \dots, \Delta\mathbf{x}_{\text{clk},s_{N_s}}^\top \right]^\top$ evolve according to the discrete-time (DT) model [36]

$$\Delta\mathbf{x}_{\text{clk}}(k+1) = \Phi_{\text{clk}}\Delta\mathbf{x}_{\text{clk}}(k) + \mathbf{w}_{\text{clk}}(k), \quad k = 0, 1, 2, \dots \quad (2)$$

$$\Phi_{\text{clk}} \triangleq \begin{bmatrix} \mathbf{F}_{\text{clk}} & \mathbf{0} & \dots & \mathbf{0} \\ \mathbf{0} & \mathbf{F}_{\text{clk}} & \dots & \mathbf{0} \\ \vdots & \vdots & \ddots & \vdots \\ \mathbf{0} & \mathbf{0} & \dots & \mathbf{F}_{\text{clk}} \end{bmatrix}, \quad \mathbf{F}_{\text{clk}} \triangleq \begin{bmatrix} 1 & T \\ 0 & 1 \end{bmatrix},$$

where k is the measurement time-step, T is the sampling time, and \mathbf{w}_{clk} is the process noise, which is modeled as a DT zero-mean white random sequence with covariance

$$\mathbf{Q}_{\text{clk}} = \boldsymbol{\Gamma} \mathbf{Q}_{\text{clk},r,s} \boldsymbol{\Gamma}^\top, \quad (3)$$

where

$$\boldsymbol{\Gamma} \triangleq \begin{bmatrix} \mathbf{I}_{2 \times 2} & -\mathbf{I}_{2 \times 2} & \mathbf{0} & \dots & \mathbf{0} \\ \mathbf{I}_{2 \times 2} & \mathbf{0} & -\mathbf{I}_{2 \times 2} & \dots & \mathbf{0} \\ \vdots & \vdots & \vdots & \ddots & \vdots \\ \mathbf{I}_{2 \times 2} & \mathbf{0} & \mathbf{0} & \dots & -\mathbf{I}_{2 \times 2} \end{bmatrix},$$

and $\mathbf{Q}_{\text{clk},r,s} \triangleq \text{diag}[\mathbf{Q}_{\text{clk},r}, \mathbf{Q}_{\text{clk},s_1}, \dots, \mathbf{Q}_{\text{clk},s_{N_s}}]$. Here, $\mathbf{Q}_{\text{clk},s_n}$ is the process noise covariance of the n -th cellular tower's clock states, which is given by

$$\mathbf{Q}_{\text{clk},s_n} = c^2 \begin{bmatrix} S_{\tilde{\omega}_{\delta t,s_n}} T + S_{\tilde{\omega}_{\delta t,s_n}} \frac{T^3}{3} & S_{\tilde{\omega}_{\delta t,s_n}} \frac{T^2}{2} \\ S_{\tilde{\omega}_{\delta t,s_n}} \frac{T^2}{2} & S_{\tilde{\omega}_{\delta t,s_n}} T \end{bmatrix},$$

where $S_{\tilde{\omega}_{\delta t,s_n}}$ and $S_{\tilde{\omega}_{\dot{\delta}t,s_n}}$ are the power spectra of the continuous-time (CT) process noise $\tilde{\omega}_{\delta t,s_n}$ and $\tilde{\omega}_{\dot{\delta}t,s_n}$, driving the clock bias and clock drift, respectively [33], [37]. Note that $\mathbf{Q}_{\text{clk},r}$ has the same form as $\mathbf{Q}_{\text{clk},s_n}$, except that $S_{\tilde{\omega}_{\delta t,s_n}}$ and $S_{\tilde{\omega}_{\dot{\delta}t,s_n}}$ are now replaced by the receiver-specific spectra $S_{\tilde{\omega}_{\delta t,r}}$ and $S_{\tilde{\omega}_{\dot{\delta}t,r}}$, respectively.

Since the cellular transmitters are assumed to be spatially-stationary, their position states evolve according to the DT dynamics

$$\mathbf{r}_s(k+1) = \mathbf{r}_s(k), \quad (4)$$

$$\text{where } \mathbf{r}_s = \left[\mathbf{r}_{s_1}^\top, \dots, \mathbf{r}_{s_{N_s}}^\top \right]^\top.$$

B. Vehicle Kinematics Model

The vehicle is assumed to be equipped with the following sensors:

- Lidar for odometry
- A receiver capable of producing pseudorange measurements to cellular towers (e.g., [22], [23])
- A GPS receiver

Vehicle's state vector \mathbf{x}_r consists of the vehicle's pose: position \mathbf{r}_r and orientation ${}^G_B \mathbf{q}$, i.e.,

$$\mathbf{x}_r \triangleq [{}^G_B \mathbf{q}^\top, \mathbf{r}_r^\top]^\top,$$

where ${}^G_B \mathbf{q}$ is the 4-D unit quaternion in vector-scalar form and represents the orientation of the vehicle body frame B with respect to the global frame G which is the Earth-centered Earth-fixed (ECEF) coordinate frame. The vector $\mathbf{r}_r = [x_r, y_r, z_r]^\top$ represents the 3-D position of the vehicle body expressed in the global frame G . The change in vehicle's states can be estimated over time using data from the lidar sensor. For this purpose, two successive lidar frames captured at time-steps k and $k+1$ are compared. Then, the change in position ${}^{B_k} \mathbf{r}_{B_{k+1}}$ and the change in orientation ${}^{B_k}_{B_{k+1}} \mathbf{q}$ of the vehicle's body frame is estimated from time-step k to time-step $k+1$. In other words, ${}^{B_k}_{B_{k+1}} \mathbf{q}$ represents the relative rotation of the vehicle body frame from time-step k to $k+1$ and ${}^{B_k} \mathbf{r}_{B_{k+1}}$ denotes the position of the vehicle at time $k+1$ expressed in the vehicle body frame at time k . Hence, the orientation of the vehicle will evolve in DT according to the kinematic model given by

$${}^{G_{k+1}} \mathbf{q} = {}^{G_{B_k}} \mathbf{q} \otimes {}^{B_k}_{B_{k+1}} \mathbf{q}, \quad (5)$$

where ${}^{G_{B_k}} \mathbf{q}$ represents the orientation of the vehicle body frame in the global frame at time k and \otimes is the quaternion multiplication operator. The vehicle's position evolves according to the kinematic model given by

$$\mathbf{r}_r(k+1) = \mathbf{r}_r(k) + \mathbf{R} [{}^G_{B_k} \mathbf{q}] {}^{B_k} \mathbf{r}_{B_{k+1}}, \quad (6)$$

where $\mathbf{R}[\mathbf{q}]$ is the 3-D rotation matrix constructed from the 4-D quaternion vector \mathbf{q} . For a sample quaternion $\mathbf{q} = [p_1 \ p_2 \ p_3 \ p_4] =$

$[p_1, p_2, p_3, p_4]^\top$, the relationship between \mathbf{q} and $\mathbf{R}[\mathbf{q}]$ is given by

$$\mathbf{R}[\mathbf{q}] = (2p_4^2)\mathbf{I}_{3 \times 3} - 2p_4[\mathbf{p} \times] + 2\mathbf{p}\mathbf{p}^\top,$$

where $[\mathbf{p} \times]$ is the skew-symmetric matrix operator, defined as

$$[\mathbf{p} \times] \triangleq \begin{bmatrix} 0 & -p_3 & p_2 \\ p_3 & 0 & -p_1 \\ -p_2 & p_1 & 0 \end{bmatrix}.$$

C. Pseudorange Observation Model

After discretization and mild approximations, the pseudoranges made by the vehicle-mounted receiver on the n -th cellular tower are given by [30], [31]

$$z_{s_n}(k) = \|\mathbf{r}_s(k) - \mathbf{r}_{s_n}(k)\|_2 + c\Delta\delta t_n(k) + v_{s_n}, \quad (7)$$

where v_{s_n} is the measurement noise, which is modeled as a DT zero-mean white Gaussian sequence with variance $\sigma_{s_n}^2$. Subsequently, the vector of pseudorange measurements to all N_s cellular tower transmitters is given by

$$\mathbf{z}_s = [z_{s_1}, \dots, z_{s_{N_s}}]^\top. \quad (8)$$

D. Lidar Measurement Model

Each lidar scan consists of relative position measurements to L points in the environment. The relative position measurement to the i -th point can be expressed as

$$\mathbf{z}_{l_i}(k) = {}^{B_k}\mathbf{r}_{l_i} + \mathbf{v}_{l_i}(k), \quad i = 1, \dots, L, \quad (9)$$

where ${}^{B_k}\mathbf{r}_{l_i}$ is the 3-D position of the i -th point expressed in the vehicle body frame at time-step k and \mathbf{v}_{l_i} is the measurement noise, which is modeled as a zero-mean Gaussian random vector with $\mathbb{E}[\mathbf{v}_{l_i}(k)\mathbf{v}_{l_i}^\top(k')] = \mathbf{C}_{l_i}\delta_{kk'}$, where $\delta_{kk'}$ is the Kronecker delta function.

III. LIDAR ODOMETRY

This section describes the steps for producing odometry measurements from lidar data using an iterative closest point (ICP) algorithm. The goal is to compare two successive point clouds captured by the lidar sensor from which to calculate the relative position ${}^{B_k}\mathbf{r}_{B_{k+1}}$ and relative orientation ${}^{B_k}_{B_{k+1}}\mathbf{q}$ of the vehicle between the lidar scan at time-step k and time-step $k + 1$. The ICP algorithm is one of the most popular methods for geometric alignment of 3-D point clouds [38], [39] and is employed for geometric alignment between two partially overlapped but misaligned data sets [40]. The ICP algorithm involves three main steps: (1) detecting feature points and eliminating remaining points, (2) finding corresponding points between two successive scans, and (3) registering the corresponding points and calculating relative rotation and translation.

A. Feature Point Extraction

In order to achieve real-time performance, the total number of points in each point cloud returned by the lidar sensor must be reduced. Moreover, since large planar areas degrade the ICP solution, it is critical to extract strategic feature points, namely sharp edges.

Edge detection algorithms are well studied in the literature [41], [42]. Let P_i be a point in a sample point cloud, and let P_i have φ nearest neighbors. Hence, there are $\varphi(\varphi-1)/2$ possible triangles with P_i and two neighboring points as vertices, and there are $\varphi(\varphi-1)/2$ unit normal vectors to these triangles. In [43], it is shown that in sharp edges, the unit normal vectors have different directions. This is illustrated in Fig. 1.

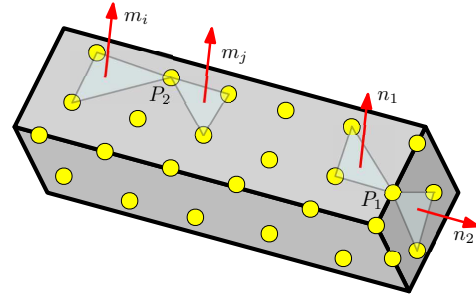


Fig. 1. An example of sharp edge extraction. The normal vectors are used for feature identification. The yellow circles are scanned point of the surface of the object. The point P_1 belongs to a sharp edge because two unequal normal vectors n_1 and n_2 are found in its neighborhood. In contrast, P_2 is not on a sharp edge because all normal vectors in its neighborhood are equal.

Since $n_1 \neq n_2$, then P_1 belongs to a sharp edge, while for all i and j in the neighborhood of P_2 , $m_i = m_j$, hence P_2 is not on a sharp edge.

Evaluating normal vectors to neighboring points is an efficient technique for extracting sharp edges. However, searching for the nearest neighbor is a time consuming step in ICP. This subsection presents a very effective technique for accelerating the search for the nearest neighbor in point clouds captured by the lidar sensor.

The points returned by the lidar sensor are stored in different layers. A layer is defined as a group of points with the same height from the ground surface. Here, it is assumed that the lidar is calibrated and mounted in parallel with the ground surface. The top layer has the maximum height with respect to the ground and the bottom layer has the minimum height with respect to the ground. In order to approximate the number of points in each layer, it is assumed that the lidar sensor produces \mathcal{P} points in each 360° scan. If the vertical field of view of the lidar is α_{min} to α_{max} degrees, and the angular resolution of scans is β degrees, then the number of points in each layer \mathcal{N}_l can be approximated to be

$$\mathcal{N}_l \approx \mathcal{P} \times \beta / (\alpha_{max} - \alpha_{min}).$$

Fig. 2 shows the points returned by a Velodyne HDL-64E lidar, which is used in the subsequent simulation and experimental results sections. It can be seen from Fig. 2 that there are exactly 1,800 points in each layer. The points returned by the lidar sensor are not stored randomly. The returned points are stored according to the lidar's electrical and mechanical scanning

steps. The lidar sensor shines a light to scan a surface, then it rotates vertically to scan another new surface. Before each rotation, the returned points from the previous scan are stored in a buffer sequentially. Subsequently, the neighboring points of P_i are limited only to the candidate points whose height or side distance are shorter than a specified threshold η with respect to P_i , i.e., P_j is a neighbor candidate of P_i if and only if

$$|i - j + \kappa \times N_l| < \eta,$$

where κ and lidar layer filter threshold η are signed and unsigned integers, respectively. For $\kappa = 0$, P_i and P_j belong to the same layer. For $\kappa = -1$, P_j belongs to an upper layer with respect to P_i , and for $\kappa = 1$, P_j belongs to a lower layer with respect to P_i . Experimental results show that $\kappa \in \{-3, -2, -1, 0, 1, 2, 3\}$ and $\eta = 10$ is a search space large enough to achieve acceptable precision.

This technique avoids searching unnecessary points. It is worth mentioning that candidate points are chosen based on their indices and there is no need for computing distances. For the lidar used in this paper, 90,000 points are returned in each scan and only 40 candidate points are evaluated.

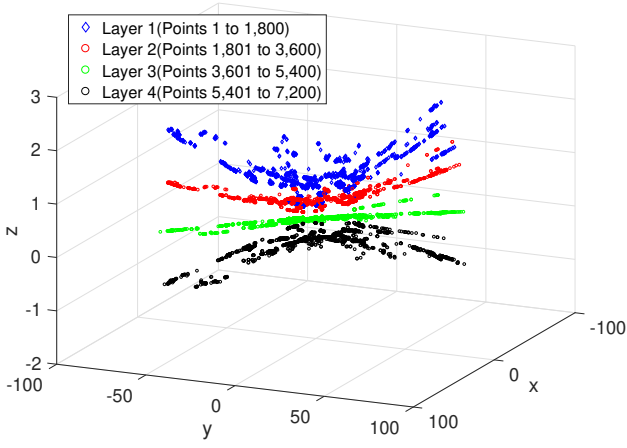


Fig. 2. The points returned by the Velodyne HDL-64E lidar. Only the first 4 layers are plotted. Each layer contains 1,800 points.

B. Finding Corresponding Points

A simple approach is used for finding corresponding points between two successive scans. In this approach [8], called mutual consistency check, given two sets of scans \mathcal{P}^k and \mathcal{P}^{k+1} , and two points $p_i^k \in \mathcal{P}^k$ and $p_{i'}^{k+1} \in \mathcal{P}^{k+1}$, then p_i^k and $p_{i'}^{k+1}$ are corresponding points if:

$$\underset{p_j^k \in \mathcal{P}^k}{\operatorname{argmin}} \|p_{i'}^{k+1} - (\mathcal{R}p_j^k + \mathcal{T})\| = p_i^k,$$

$$\underset{p_j^{k+1} \in \mathcal{P}^{k+1}}{\operatorname{argmin}} \|p_i^k - [\mathcal{R}^\top (p_j^{k+1} - \mathcal{T})]\| = p_{i'}^{k+1},$$

where \mathcal{R} is the rotation matrix and \mathcal{T} is the translation vector obtained from the last odometry measurement in which \mathcal{P}^{k-1} and \mathcal{P}^k were processed. Due to the large mass and inertia of the vehicle, \mathcal{R} and \mathcal{T} do not change significantly

from time-step k to $k + 1$. This causes fast convergence of the ICP algorithm, which was noticed with simulation and experimental results.

C. Point Registration

In the point registration step, the algorithm estimates the relative change in the vehicle position ${}^{B_k}\mathbf{r}_{B_{k+1}}$ and orientation ${}^{B_k}_{B_{k+1}}\mathbf{q}$. This is achieved by solving for the transformation (rotation and translation) between two lidar point clouds. There are several methods to perform point registration. In [32], a maximum likelihood approach for registering the points was presented. In this method, the relative change in position and orientation of the vehicle is estimated iteratively using the Gauss-Newton method, until the estimates converge. The estimates are updated after each iteration according to

$${}^{B_k}\hat{\mathbf{r}}_{B_{k+1}}^{(t+1)} = {}^{B_k}\hat{\mathbf{r}}_{B_{k+1}}^{(t)} + {}^{B_k}\tilde{\mathbf{r}}_{B_{k+1}}^{(t)},$$

$${}^{B_k}_{B_{k+1}}\hat{\mathbf{q}}^{(t+1)} = {}^{B_k}_{B_{k+1}}\tilde{\mathbf{q}}^{(t)} \otimes {}^{B_k}_{B_{k+1}}\hat{\mathbf{q}}^{(t)},$$

where

$${}^{B_k}_{B_{k+1}}\tilde{\mathbf{q}}^{(t)} \triangleq \left[\frac{1}{2} \left(\tilde{\boldsymbol{\theta}}_l^{(t)} \right)^\top, \sqrt{1 - \frac{1}{4} \left(\tilde{\boldsymbol{\theta}}_l^{(t)} \right)^\top \tilde{\boldsymbol{\theta}}_l^{(t)}} \right]^\top,$$

$\tilde{\boldsymbol{\theta}}_l^{(t)}$ and ${}^{B_k}\tilde{\mathbf{r}}_{B_{k+1}}^{(t)}$ are the corrections computed at iteration t according to

$$\begin{bmatrix} \tilde{\boldsymbol{\theta}}_l^{(t)} \\ {}^{B_k}\tilde{\mathbf{r}}_{B_{k+1}}^{(t)} \end{bmatrix} = \mathbf{Q}_l^{(t)} \left[\sum_{i=1}^{N_p} \left(\mathbf{H}_{l_i}^{(t)} \right)^\top \left(\mathbf{C}_{n_i}^{(t)}(k) \right)^{-1} \mathbf{v}_{l_i}(k) \right],$$

$$\mathbf{Q}_l^{(t)} = \left[\sum_{i=1}^{N_p} \left(\mathbf{H}_{l_i}^{(t)} \right)^\top \left(\mathbf{C}_{n_i}^{(t)}(k) \right)^{-1} \mathbf{H}_{l_i}^{(t)} \right]^{-1},$$

$$\mathbf{H}_{l_i}^{(t)} = \left[-[\mathbf{R} \left[{}^{B_k}_{B_{k+1}}\hat{\mathbf{q}}^{(t)} \right] \mathbf{z}_{l_i}(k+1) \times] \quad \mathbf{I} \right],$$

$$\mathbf{C}_{n_i}(k) = \mathbf{C}_{l_i} + \mathbf{R} \left[{}^{B_k}_{B_{k+1}}\hat{\mathbf{q}} \right] \mathbf{C}_{l_i} \mathbf{R} \left[{}^{B_k}_{B_{k+1}}\hat{\mathbf{q}} \right]^\top,$$

where $\mathbf{z}_{l_i}(k)$ and \mathbf{C}_{l_i} are obtained according to (9). After convergence, an estimate $\hat{\mathbf{x}}_l = \left[{}^{B_k}_{B_{k+1}}\hat{\mathbf{q}}^\top, {}^{B_k}\hat{\mathbf{r}}_{B_{k+1}}^\top \right]^\top$ is obtained. The resulting estimation error $\tilde{\mathbf{x}}_l = \left[\tilde{\boldsymbol{\theta}}_l^\top, {}^{B_k}\tilde{\mathbf{r}}_{B_{k+1}}^\top \right]^\top$ is zero-mean and has a covariance \mathbf{Q}_l . The proposed approach also estimates the covariance of the relative pose estimation error. This will be useful when propagating the covariance of the absolute pose estimation error in the EKF.

Fig. 3 summarizes all the steps of the proposed computationally efficient odometry measurement extraction method.

IV. POSE ESTIMATION USING CELLULAR PSEUDORANGES

In this section, an approach to extract 3-D position information from pseudorange measurements from unknown cellular towers is proposed.

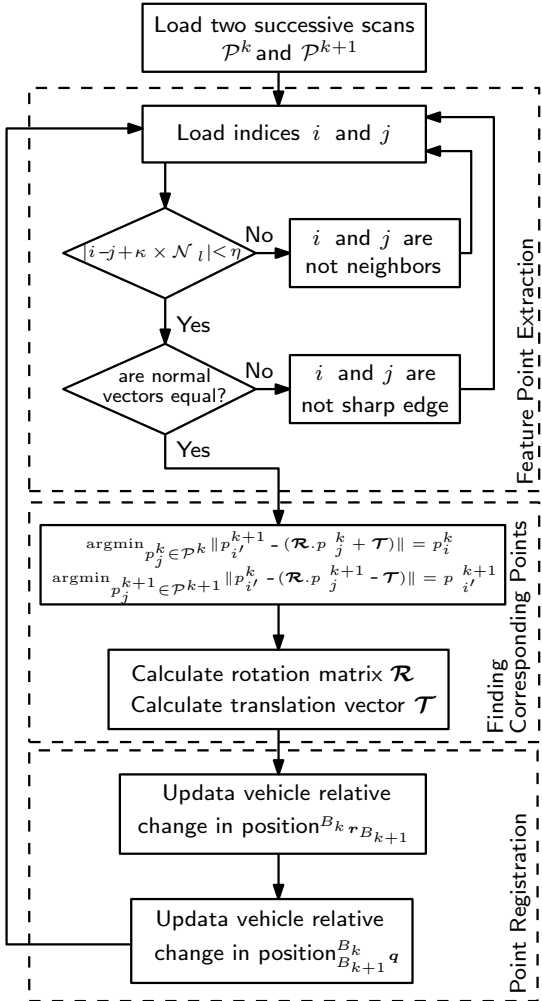


Fig. 3. Step-by-step summary of the proposed computationally efficient odometry measurement extraction method. The proposed method consists of three parts: feature point extraction, finding corresponding points, and point registration.

A. Problem Formulation

The vehicle is assumed to navigate in an environment comprising N_s cellular transmitters. The states of these transmitters are assumed to be unknown. When GNSS signals are available, the vehicle could estimate its own states and starts mapping the cellular transmitters' states, i.e., estimating their position and clock bias and drift from the pseudorange measurements produced by the receiver. When GNSS signals become unavailable, the vehicle enters the SLAM mode. Here, the vehicle uses lidar for odometry, continues mapping the cellular transmitters' states, and simultaneously localizes itself (estimating its own position and orientation).

The cellular towers are analogous to the landmarks in the SLAM problem, with the added complexity of estimating the dynamic and stochastic clock error states of each cellular tower. To tackle this problem, an EKF-based framework is adopted that operates in (1) a mapping mode when GNSS signals are available and (2) a SLAM mode when the GNSS signals are unavailable. A depiction of this framework is illustrated in Fig. 4. The following subsections detail the operations of each mode.

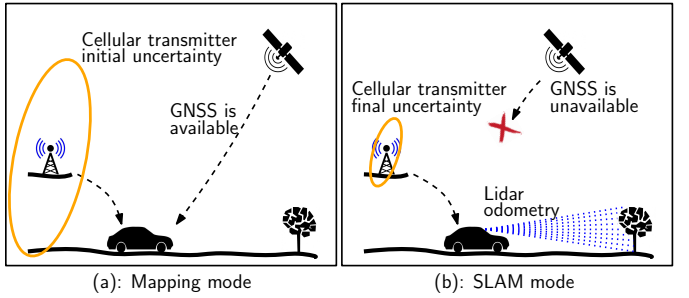


Fig. 4. Proposed pose estimation framework. (a) Mapping mode: the vehicle's state is known from available GNSS signals. The vehicle fuses pseudoranges made on the cellular transmitter to map the transmitters' state. (b) SLAM mode: GNSS signals are unavailable. Here, the vehicle maps the cellular transmitter states, simultaneously with localizing itself, while using pseudorange measurements from the mapped cellular towers as aiding source to correct the lidar's accumulated errors.

B. Mapping Mode

This subsection describes the EKF calculations during the mapping mode. In this mode, the vehicle-mounted receiver has access to GNSS, from which it could estimate its position state \mathbf{r}_r . The EKF state vector \mathbf{x} comprises the cellular tower locations and the difference between the receiver's and cellular transmitters' clock bias and drift, namely

$$\mathbf{x} = [\mathbf{r}_{s1}^\top, \dots, \mathbf{r}_{sn}^\top, \Delta \mathbf{x}_{clk,s_1}^\top, \dots, \Delta \mathbf{x}_{clk,s_{N_s}}^\top]^\top. \quad (10)$$

The estimation framework in the mapping mode is illustrated in Fig. 5

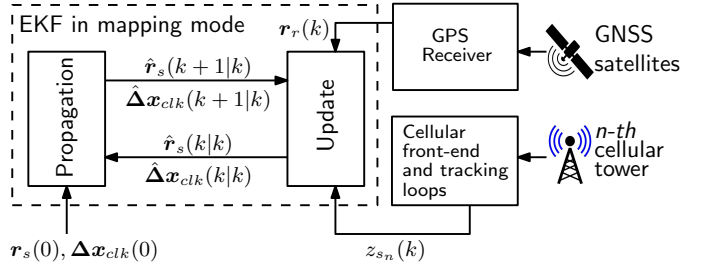


Fig. 5. Framework for mapping the cellular transmitters in the environment during the mapping mode.

The dynamics discussed in section II-A are used to calculate the predicted state estimate $\hat{\mathbf{x}}(k+1|k)$ and associated prediction error covariance $\mathbf{P}(k+1|k)$ according to

$$\hat{\mathbf{x}}(k+1|k) = \mathbf{F}\hat{\mathbf{x}}(k|k),$$

$$\mathbf{P}(k+1|k) = \mathbf{F}\mathbf{P}(k|k)\mathbf{F}^\top + \begin{bmatrix} \mathbf{0}_{3N_s \times 3N_s} & \mathbf{0} \\ \mathbf{0} & \mathbf{Q}_{clk} \end{bmatrix},$$

where

$$\mathbf{F} = \begin{bmatrix} \mathbf{I}_{3N_s \times 3N_s} & \mathbf{0} \\ \mathbf{0} & \mathbf{\Phi}_{clk} \end{bmatrix}.$$

Given the vehicle's position $\mathbf{r}_r(k+1)$ from the GNSS receiver, the measurement prediction $\hat{z}_{s_n}(k+1|k)$ can be computed as

$$\begin{aligned} \hat{z}_{s_n}(k+1|k) &= \|\mathbf{r}_r(k+1) - \hat{\mathbf{r}}_{s_n}(k+1|k)\|_2 \\ &\quad + c\hat{\Delta}\delta t_n(k+1|k), \quad n = 1, \dots, N_s. \end{aligned} \quad (11)$$

Given cellular pseudorange measurements $z_s(k+1)$ the innovation $\nu_s(k+1)$ is computed as

$$\nu_s(k+1) = z_s(k+1) - \hat{z}_s(k+1|k),$$

where

$$\hat{z}_s(k+1|k) \triangleq [\hat{z}_{s_1}(k+1|k), \dots, \hat{z}_{s_{N_s}}(k+1|k)]^\top.$$

The corresponding measurement Jacobian $\mathbf{H}(k+1) \triangleq \frac{\partial z_s(k+1)}{\partial \mathbf{x}(k+1)}$ is given by

$$\mathbf{H}(k+1) = [\mathbf{H}_{\text{rs}} \quad \mathbf{H}_{\text{clk}}], \quad (12)$$

where

$$\begin{aligned} \mathbf{H}_{\text{rs}} &= \text{diag}[\mathbf{1}_{s_1}^\top, \dots, \mathbf{1}_{s_{N_s}}^\top], \\ \mathbf{1}_{s_n} &= \frac{\hat{\mathbf{r}}_{s_n}(k+1|k) - \mathbf{r}_r(k+1)}{\|\hat{\mathbf{r}}_{s_n}(k+1|k) - \mathbf{r}_r(k+1)\|_2}, \end{aligned}$$

and

$$\mathbf{H}_{\text{clk}} = \text{diag}[\mathbf{h}_{\text{clk},s_1}, \dots, \mathbf{h}_{\text{clk},s_{N_s}}], \quad \mathbf{h}_{\text{clk},s_n} = [1 \quad 0].$$

Note that $\mathbf{1}_{s_n}$ is the unit line-of-sight vector between the receiver and the n -th cellular transmitter, expressed in the ECEF coordinate frame. The Kalman gain $\mathbf{K}(k+1)$ is computed according to

$$\mathbf{K}(k+1) = \mathbf{P}(k+1|k)\mathbf{H}(k+1)^\top \mathbf{S}(k+1)^{-1},$$

where $\mathbf{S}(k+1) = \mathbf{H}(k+1)\mathbf{P}(k+1|k)\mathbf{H}(k+1)^\top + \Sigma_s$ is the innovation covariance and $\Sigma_s = \text{diag}[\sigma_{s_1}^2, \dots, \sigma_{s_{N_s}}^2]$ is the measurement noise covariance.

The cellular transmitter's corrected state estimate $\hat{\mathbf{x}}(k+1|k+1)$ and associated estimation error covariance is computed from

$$\hat{\mathbf{x}}(k+1|k+1) = \hat{\mathbf{x}}(k+1|k) + \mathbf{K}(k+1)\nu_s(k+1|k),$$

$$\mathbf{P}(k+1|k+1) = [\mathbf{I} - \mathbf{K}(k+1)\mathbf{H}(k+1)]\mathbf{P}(k+1|k).$$

C. SLAM Mode

This subsection describes the EKF calculations during the SLAM mode. In this mode, the vehicle-mounted receiver has no access to GNSS signals. The EKF estimate the cellular towers' state simultaneously with the vehicle's own state. The estimation framework in the SLAM mode is illustrated in Fig. 6. At each time-step k , the proposed ICP algorithm produces the relative pose ${}^{B_k}\hat{\mathbf{r}}_{B_{k+1}}$ and relative orientation ${}^{B_k}\hat{\mathbf{q}}_{B_{k+1}}$ of the vehicle between two consecutive lidar scans, which are used to propagate the states of the receiver. Then, the pseudoranges are used to update the receiver's pose estimate as well as the cellular towers' position and clock state estimates.

In order to differentiate between the mapping and SLAM modes, the “prime” symbol is used to designate the variables in the SLAM mode throughout this subsection. Therefore, “ x ” is now replaced with “ x' ”. The state vector x' comprises the vehicle's pose (position and orientation), cellular towers' position, and the difference between the receiver's and the cellular transmitters' clock bias and drift, namely

$$x' = \left[{}^G_B \mathbf{q}^\top, \mathbf{r}_r^\top, \Delta \mathbf{x}_{\text{clk},s_1}^\top, \dots, \Delta \mathbf{x}_{\text{clk},s_{N_s}}^\top, \mathbf{r}_{s_1}^\top, \dots, \mathbf{r}_{s_{N_s}}^\top \right]^\top,$$

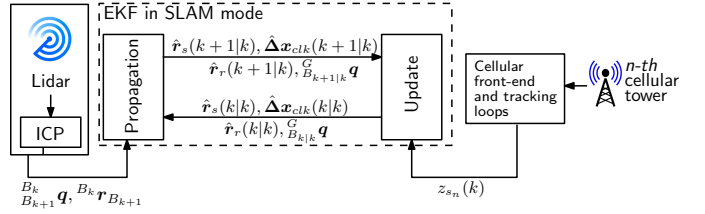


Fig. 6. Framework for mapping the cellular towers in the environment simultaneously with localizing the vehicle.

The EKF error state is defined as

$$\tilde{\mathbf{x}}' \triangleq \left[\tilde{\theta}^\top, \tilde{\mathbf{r}}_r^\top, \tilde{\Delta \mathbf{x}}_{\text{clk},s_1}^\top, \dots, \tilde{\Delta \mathbf{x}}_{\text{clk},s_{N_s}}^\top, \tilde{\mathbf{r}}_{s_1}^\top, \dots, \tilde{\mathbf{r}}_{s_{N_s}}^\top \right]^\top,$$

where $\tilde{\theta}$ is the 3-axis angle error vector. Note that the quaternion representation is an over-determined representation of the orientation of a body. Hence, the estimation error covariance associated with the quaternion estimate will always be singular. To avoid singularity, the vector of angle errors $\tilde{\theta}$ is used to form the error state vector. The orientation error model follows the quaternion multiplication model given by

$${}^G_B \mathbf{q} = \delta \mathbf{q} \otimes {}^G_B \hat{\mathbf{q}},$$

where

$$\delta \mathbf{q} = \left[\frac{1}{2} \tilde{\theta}^\top, \sqrt{1 - \frac{1}{4} \tilde{\theta}^\top \tilde{\theta}} \right]^\top.$$

The position and clock errors are defined using the standard additive error model

$$\begin{aligned} \tilde{\mathbf{r}}_r &= \mathbf{r}_r - \hat{\mathbf{r}}_r, \\ \tilde{\Delta \mathbf{x}}_{\text{clk},s_n} &= \Delta \mathbf{x}_{\text{clk},s_n} - \hat{\Delta \mathbf{x}}_{\text{clk},s_n}, \quad n = 1, \dots, N_s, \\ \tilde{\mathbf{r}}_{s_n} &= \mathbf{r}_{s_n} - \hat{\mathbf{r}}_{s_n}, \quad n = 1, \dots, N_s. \end{aligned} \quad (13)$$

In the SLAM mode, the propagation of the state estimate follows directly from (2) and (4)-(6) and is given by

$$\begin{aligned} {}^{B_{k+1|k}} \hat{\mathbf{q}} &= {}^{B_{k|k}} \hat{\mathbf{q}} \otimes {}^{B_k}_{B_{k+1}} \hat{\mathbf{q}}, \\ \hat{\mathbf{r}}_r(k+1|k) &= \hat{\mathbf{r}}_r(k|k) + \mathbf{R} \left[{}^G_{B_{k|k}} \hat{\mathbf{q}} \right] {}^{B_k} \hat{\mathbf{r}}_{B_{k+1}}, \\ \hat{\Delta \mathbf{x}}_{\text{clk}}(k+1|k) &= \Phi_{\text{clk}} \hat{\Delta \mathbf{x}}_{\text{clk}}(k|k), \\ \hat{\mathbf{r}}_s(k+1|k) &= \hat{\mathbf{r}}_s(k|k). \end{aligned} \quad (14)$$

In order to obtain the propagation equation for the estimation error covariance, the linearized error dynamics are first derived. The orientation propagation equation in (5) may be expressed as

$$\mathbf{R} \left[{}^G_{B_{k+1}} \mathbf{q} \right] = \mathbf{R} \left[{}^G_{B_k} \mathbf{q} \right] \mathbf{R} \left[{}^{B_k}_{B_{k+1}} \mathbf{q} \right]. \quad (15)$$

Using the small angle approximation, (15) can be approximated with

$$\begin{aligned} &\left(\mathbf{I} + [\tilde{\theta}(k+1|k) \times] \right) \mathbf{R} \left[{}^G_{B_{k+1|k}} \hat{\mathbf{q}} \right] \\ &\approx \left(\mathbf{I} + [\tilde{\theta}(k|k) \times] \right) \mathbf{R} \left[{}^G_{B_{k|k}} \hat{\mathbf{q}} \right] \left(\mathbf{I} + [\tilde{\theta}_l(k) \times] \right) \mathbf{R} \left[{}^{B_k}_{B_{k+1}} \hat{\mathbf{q}} \right], \end{aligned}$$

where $\tilde{\theta}_l(k)$ is the error from the ICP algorithm for estimating the relative change in the orientation of the vehicle ${}^{B_k}_{B_{k+1}}\hat{q}$ at time-step k . The above equation becomes

$$\begin{aligned} & \mathbf{R} \left[{}^G_{B_{k+1|k}} \hat{q} \right] + [\tilde{\theta}(k+1|k) \times] \mathbf{R} \left[{}^G_{B_{k+1|k}} \hat{q} \right] \\ & \approx \mathbf{R} \left[{}^G_{B_{k|k}} \hat{q} \right] \mathbf{R} \left[{}^{B_k}_{B_{k+1}} \hat{q} \right] + [\tilde{\theta}(k|k) \times] \mathbf{R} \left[{}^G_{B_{k|k}} \hat{q} \right] \mathbf{R} \left[{}^{B_k}_{B_{k+1}} \hat{q} \right] \\ & \quad + \mathbf{R} \left[{}^G_{B_{k|k}} \hat{q} \right] [\tilde{\theta}_l(k) \times] \mathbf{R} \left[{}^{B_k}_{B_{k+1}} \hat{q} \right] \\ & \quad + \underbrace{[\tilde{\theta}(k|k) \times] \mathbf{R} \left[{}^G_{B_{k|k}} \hat{q} \right] [\tilde{\theta}_l(k) \times] \mathbf{R} \left[{}^{B_k}_{B_{k+1}} \hat{q} \right]}_{\approx 0}. \end{aligned}$$

Since $\mathbf{R}[a \times] \mathbf{R}^\top = [Ra \times]$, then the orientation equation becomes

$$\begin{aligned} & \mathbf{R} \left[{}^G_{B_{k+1|k}} \hat{q} \right] + [\tilde{\theta}(k+1|k) \times] \mathbf{R} \left[{}^G_{B_{k+1|k}} \hat{q} \right] \\ & \approx \mathbf{R} \left[{}^G_{B_{k+1|k}} \hat{q} \right] + [\tilde{\theta}(k|k) \times] \mathbf{R} \left[{}^G_{B_{k+1|k}} \hat{q} \right] \\ & \quad + \mathbf{R} \left[{}^G_{B_{k|k}} \hat{q} \right] [\tilde{\theta}_l(k) \times] \mathbf{R} \left[{}^{B_k}_{B_{k+1}} \hat{q} \right]. \end{aligned}$$

Right-multiplying both sides by $\mathbf{R}^\top \left[{}^G_{B_{k+1|k}} \hat{q} \right]$ yields

$$[\tilde{\theta}(k+1|k) \times] \approx [\tilde{\theta}(k|k) \times] + \mathbf{R} \left[{}^G_{B_{k|k}} \hat{q} \right] [\tilde{\theta}_l(k) \times] \mathbf{R}^\top \left[{}^G_{B_{k|k}} \hat{q} \right];$$

hence,

$$\tilde{\theta}(k+1|k) \approx \tilde{\theta}(k|k) + \mathbf{R} \left[{}^G_{B_{k|k}} \hat{q} \right] \tilde{\theta}_l(k). \quad (16)$$

The receiver position propagation equation in (6) can be approximated with

$$\begin{aligned} & \hat{r}_r(k+1|k) + \tilde{r}_r(k+1|k) \approx \hat{r}_r(k|k) + \tilde{r}_r(k|k) \\ & + (\mathbf{I} + [\tilde{\theta}(k|k) \times]) \mathbf{R} \left[{}^G_{B_{k|k}} \hat{q} \right] ({}^{B_k} \hat{r}_{B_{k+1}} + {}^{B_k} \tilde{r}_{B_{k+1}}), \end{aligned}$$

which becomes

$$\begin{aligned} & \hat{r}_r(k+1|k) + \tilde{r}_r(k+1|k) \\ & \approx \tilde{r}_r(k|k) + \mathbf{R} \left[{}^G_{B_{k|k}} \hat{q} \right] {}^{B_k} \tilde{r}_{B_{k+1}} \\ & \quad + [\tilde{\theta}(k|k) \times] \mathbf{R} \left[{}^G_{B_{k|k}} \hat{q} \right] {}^{B_k} \hat{r}_{B_{k+1}} \\ & \quad + \underbrace{[\tilde{\theta}(k|k) \times] \mathbf{R} \left[{}^G_{B_{k|j}} \hat{q} \right] {}^{B_k} \tilde{r}_{B_{k+1}}}_{\approx 0} \\ & \quad + \hat{r}_r(k|k) + \underbrace{\mathbf{R} \left[{}^G_{B_{k|k}} \hat{q} \right] {}^{B_k} \hat{r}_{B_{k+1}}}_{=\hat{r}_r(k+1|k)}. \end{aligned}$$

Since $[a \times] b = -[b \times] a$, then the position error dynamics may be expressed as

$$\begin{aligned} \tilde{r}_r(k+1|k) & \approx \tilde{r}_r(k|k) - [\mathbf{R} \left[{}^G_{B_{k|k}} \hat{q} \right] {}^{B_k} \hat{r}_{B_{k+1}} \times] \tilde{\theta}(k|k) \\ & \quad + \mathbf{R} \left[{}^G_{B_{k|k}} \hat{q} \right] {}^{B_k} \tilde{r}_{B_{k+1}}. \end{aligned} \quad (17)$$

Therefore, the prediction state estimate of the error state is given by

$$\begin{bmatrix} \tilde{\theta}(k+1|k) \\ \tilde{r}_r(k+1|k) \\ \tilde{\Delta x}_{\text{clk}}(k+1|k) \\ \tilde{r}_s(k+1|k) \end{bmatrix} \approx \mathbf{F}' \begin{bmatrix} \tilde{\theta}(k|k) \\ \tilde{r}_r(k|k) \\ \tilde{\Delta x}_{\text{clk}}(k|k) \\ \tilde{r}_s(k|k) \end{bmatrix} + \Psi' \begin{bmatrix} \tilde{\theta}_l(k) \\ {}^{B_k} \tilde{r}_{B_{k+1}} \\ \mathbf{0} \\ \mathbf{0} \end{bmatrix},$$

where

$$\begin{aligned} \mathbf{F}' &= \text{diag} [\Phi_R, \Phi_{\text{clk}}, \mathbf{I}_{3N_s \times 3N_s}], \\ \Psi' &= \text{diag} \left[\mathbf{R} \left[{}^G_{B_{k|k}} \hat{q} \right], \mathbf{R} \left[{}^G_{B_{k|k}} \hat{q} \right], \mathbf{I}_{5N_s \times 5N_s} \right], \\ \Phi_R &= \begin{bmatrix} \mathbf{I} & \mathbf{0} \\ -[\mathbf{R} \left[{}^G_{B_{k|k}} \hat{q} \right] {}^{B_k} \hat{r}_{B_{k+1}} \times] & \mathbf{I} \end{bmatrix}. \end{aligned}$$

The corresponding prediction estimation error covariance is given by

$$\begin{aligned} \mathbf{P}'(k+1|k) &= \\ \mathbf{F}' \mathbf{P}'(k+1|k) \mathbf{F}'^\top + \Psi' & \begin{bmatrix} \mathbf{Q}_l & \mathbf{0} & \mathbf{0} \\ \mathbf{0} & \mathbf{Q}_{\text{clk}} & \mathbf{0} \\ \mathbf{0} & \mathbf{0} & \mathbf{0}_{3N_s \times 3N_s} \end{bmatrix} \Psi'^\top. \end{aligned}$$

Given the predicted estimation $\hat{r}_r(k+1|k)$, $\hat{r}_{s,n}(k+1|k)$, and $c\hat{\Delta}\delta t_n(k+1|k)$, the measurement prediction is computed from

$$\begin{aligned} \hat{z}_{s,n}(k+1|k) &= \|\hat{r}_r(k+1|k) - \hat{r}_{s,n}(k+1|k)\|_2 \\ & + c\hat{\Delta}\delta t_n(k+1|k), \quad n = 1, \dots, N_s. \end{aligned}$$

Given cellular pseudorange measurements $\mathbf{z}_s(k+1)$ the innovation $\boldsymbol{\nu}_s(k+1)$ is subsequently computed. The measurement Jacobian in the SLAM mode takes the form

$$\mathbf{H}'(k+1) = [\mathbf{H}'_{\text{rr}, \text{rs}} \quad \mathbf{H}_{\text{clk}} \quad \mathbf{H}'_{\text{rs}, \text{rr}}],$$

where:

$$\mathbf{H}'_{\text{rr}, \text{rs}} = [h'_1, \dots, h'_{N_s}]^\top,$$

$$h'_n = \begin{bmatrix} \mathbf{0}_{1 \times 3} & -\mathbf{1}'_{s_n}^\top \end{bmatrix}^\top, \quad n = 1, \dots, N_s,$$

$$\mathbf{H}'_{\text{rs}, \text{rr}} = \text{diag} [\mathbf{1}'_{s_1}^\top, \dots, \mathbf{1}'_{s_{N_s}}^\top],$$

$$\mathbf{1}'_{s_n} = \frac{\hat{r}_{s,n}(k+1|k) - \hat{r}_r(k+1|k)}{\|\hat{r}_r(k+1|k) - \hat{r}_{s,n}(k+1|k)\|_2}, \quad n = 1, \dots, N_s.$$

The Kalman gain $\mathbf{K}'(k+1)$ is computed according to

$$\mathbf{K}'(k+1) = \mathbf{P}'(k+1|k) \mathbf{H}'(k+1)^\top \mathbf{S}'(k+1)^{-1},$$

where $\mathbf{S}'(k+1) = \mathbf{H}'(k+1) \mathbf{P}'(k+1|k) \mathbf{H}'(k+1)^\top + \boldsymbol{\Sigma}_s$ is the innovation covariance and $\boldsymbol{\Sigma}_s = \text{diag} [\sigma_{s_1}^2, \dots, \sigma_{s_{N_s}}^2]$ is the measurement noise covariance.

The corrected state in the SLAM mode is more complex than the one in the mapping mode because of the orientation state. Define

$$\boldsymbol{\xi} \triangleq \mathbf{K}'(k+1) \boldsymbol{\nu}(k+1|k) \triangleq \begin{bmatrix} \xi_\theta \\ \xi_{r_r} \\ \xi_{\Delta x_{\text{clk}}} \\ \xi_{r_s} \end{bmatrix},$$

where the elements of $\boldsymbol{\xi}$ denote the receiver's orientation, receiver's position, difference between the receiver's and cellular transmitters' clock bias and drift, and cellular tower's position corrections, respectively. Subsequently, the following update equations are obtained

$$\begin{bmatrix} \hat{r}_r(k+1|k+1) \\ \tilde{\Delta x}_{\text{clk}}(k+1|k+1) \\ \hat{r}_s(k+1|k+1) \end{bmatrix} = \begin{bmatrix} \hat{r}_r(k+1|k) \\ \tilde{\Delta x}_{\text{clk}}(k+1|k) \\ \hat{r}_s(k+1|k) \end{bmatrix} + \begin{bmatrix} \xi_{r_r} \\ \xi_{\Delta x_{\text{clk}}} \\ \xi_{r_s} \end{bmatrix},$$

and

$${}^G_B_{k+1|k+1} \hat{\mathbf{q}} = {}^G_B_{k+1|k} \hat{\mathbf{q}} \otimes \delta \mathbf{q}_\xi,$$

where

$$\delta \mathbf{q}_\xi = \left[\frac{1}{2} \boldsymbol{\xi}_\theta^\top, \sqrt{1 - \frac{1}{4} \boldsymbol{\xi}_\theta^\top \boldsymbol{\xi}_\theta} \right]^\top.$$

The corresponding estimation error covariance is given by

$$\mathbf{P}'(k+1|k+1) = [\mathbf{I} - \mathbf{K}'(k+1)\mathbf{H}'(k+1)]\mathbf{P}'(k+1|k).$$

V. SIMULATION RESULTS

This section presents simulation results demonstrating the performance of the framework described in Section IV. The simulator used ground truth and real lidar data from the KITTI data benchmark [35]. The simulator generated (1) the states of the vehicle-mounted receiver, (2) the cellular towers' states, and (3) pseudorange measurements made by the vehicle-mounted receiver on the cellular towers. The estimation error of cellular-aided navigation solution is compared with the ICP-only solution. Moreover, the position estimation of the cellular towers are evaluated.

A. Data set Description

A data set from the KITTI benchmark is used to perform the simulation test. The KITTI Vision Benchmark Suite is a public computer vision and robotic algorithm benchmarking data set which covers different types of environments, including urban and suburban areas in the city of Karlsruhe, Germany. Fig. 7. shows the recording platform and sensor setup which has been used to record the data set. Fig. 7 also shows a top view of a point cloud taken from an intersection and the corresponding visual image. The blue point cloud contains all points captured by the lidar and the black point cloud represents corresponding edges and feature points. Each laser scan returns around 120,000 points in 3-D space. To enable real-time processing, the proposed framework uses only 2.5% of the total points in each scan. The KITTI benchmark also provides the GPS-IMU data, which is assumed to be the ground truth.

B. Scenario Description

Four different trajectories from the KITTI benchmark were processed (i.e., Test 1–4). Pseudoranges from a varying number of cellular towers were simulated. The cellular towers were assumed to be equipped with oven-controlled crystal oscillators (OCXO), while the vehicle-mounted receiver was assumed to be equipped with a temperature-compensated crystal oscillator (TCXO). The simulation settings are summarized in Table I.

The vehicle was assumed to know its state and be in the mapping mode only for the first 5 seconds. Then, the vehicle was assumed to loose access to GNSS signals and entered the SLAM mode. The EKF of the mapping mode was initiated with $\hat{\mathbf{r}}_{s_n}(0|-1) \sim \mathcal{N}[\mathbf{r}_{s_n}(0), \mathbf{P}_{r_{s_n}}(0|-1)]$, where $\mathbf{P}_{r_{s_n}}(0|-1) \equiv (10^6) \cdot \text{diag}[1, 1, 1]$, for $n = 1, \dots, N_s$ and $\hat{\Delta \mathbf{x}}_{\text{clk}, s_n}(0|-1) \sim \mathcal{N}[\Delta \mathbf{x}_{\text{clk}, s_n}(0), \mathbf{P}_{\text{clk}, s_n}(0|-1)]$, where $\mathbf{P}_{\text{clk}, s_n}(0|-1) \equiv (10^4) \cdot \text{diag}[3, 0.3]$.

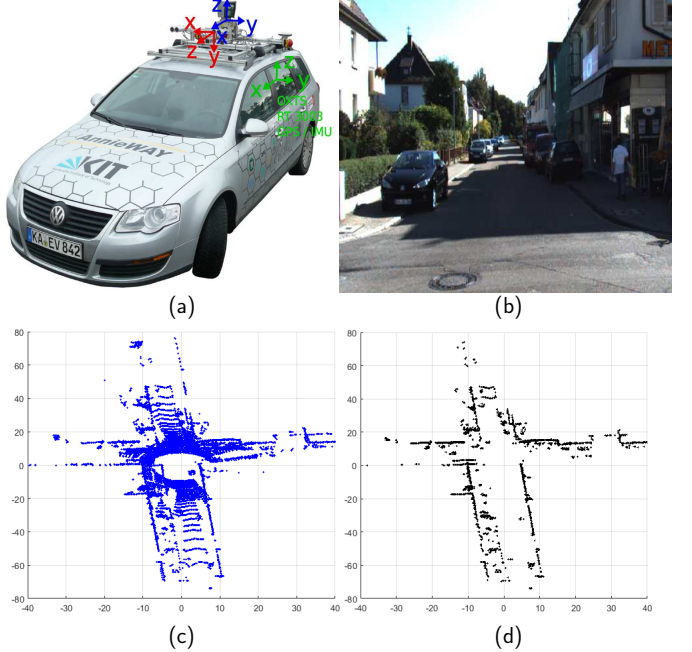


Fig. 7. (a) Sensor configuration and vehicle used by KITTI. The vehicle is equipped with a lidar, a camera, and an integrated GPS-IMU system which is used for ground truth acquisition [44]. (b) Example environment in which the vehicle used by KITTI was driven for data collection [44]. (c) A sample point cloud of the data from the KITTI data set [35]. (d) Feature points and detected edges produced by the proposed algorithm discussed in Fig. 3 for the point cloud in (c). Each laser scan returns around 120,000 points in 3-D space. To enable real-time processing, the proposed framework uses only 2.5% of the total points in each scan.

TABLE I
SIMULATION SETTINGS

Parameter	Definition	Value
r_r	Vehicle's initial position	$[0, 0, 0]^\top$ m
N_s	Number of towers	2–5
T	Sampling time	0.1 s
$\sigma_{s_n}^2$	Measurement noise variance	10 m^2
$\{S_{\tilde{\omega}_{\delta t, s_n}}\}_{n=1}^{N_s}$	Clock bias process noise power spectral density of transmitters	$4 \times 10^{-20} \text{ s}$
$\{S_{\tilde{\omega}_{\delta t, s_n}}\}_{n=1}^{N_s}$	Clock drift process noise power spectral density of transmitters	$7.89 \times 10^{-22} \text{ 1/s}$
$S_{\tilde{\omega}_{\delta t, r}}$	Clock bias process noise power spectral density of the receiver	$4.7 \times 10^{-20} \text{ s}$
$S_{\tilde{\omega}_{\delta t, r}}$	Clock drift process noise power spectral density of the receiver	$7.5 \times 10^{-20} \text{ 1/s}$
κ	Lidar nearest neighbor layers	$\{-2, -1, 0, 1, 2\}$
η	Lidar layer filter threshold	1
r_{s_1}	Tower 1 location	$[-2100, 1900, 0]^\top$ m
r_{s_2}	Tower 2 location	$[2000, 2500, 0]^\top$ m
r_{s_3}	Tower 3 location	$[900, -2300, 0]^\top$ m
r_{s_4}	Tower 4 location	$[3100, 1500, 0]^\top$ m
r_{s_5}	Tower 5 location	$[1000, 1000, 0]^\top$ m

C. Navigation Results

The true trajectories by the vehicle for the four KITTI data sets are illustrated in Fig. 8. Also, shown in Fig. 8 are the ICP-

only lidar estimated trajectory and the proposed cellular-aided lidar trajectory. It is worth noting that 95% of the traversed trajectory in Fig. 8 was without GNSS. It is evident from Fig. 8 that the cellular-aided lidar trajectory closely matched the true trajectory, while the ICP-only lidar trajectory drifted from the true trajectory. Lidar-based navigation frameworks studied in literature achieve position accuracy within a lane-level [45]. However, in this simulation, only 2.5% of the total scanned points were used in the ICP algorithm, causing a significant drift in the ICP-only solution. It can be seen from Fig. 8(e) that using only 2.5% of the scanned points degrades the ICP-only solution dramatically.

The performance of the proposed framework is compared with both the ICP-only and cellular-only navigation frameworks. Table II summarized the position RMSE with the ICP-only method, cellular-only method, and the proposed cellular-aided lidar method. These results correspond to the KITTI data set scenarios described in Subsection V-B. The reduction in the estimation error upon fusing lidar data with cellular pseudoranges is significant and the estimates are at the lane-level.

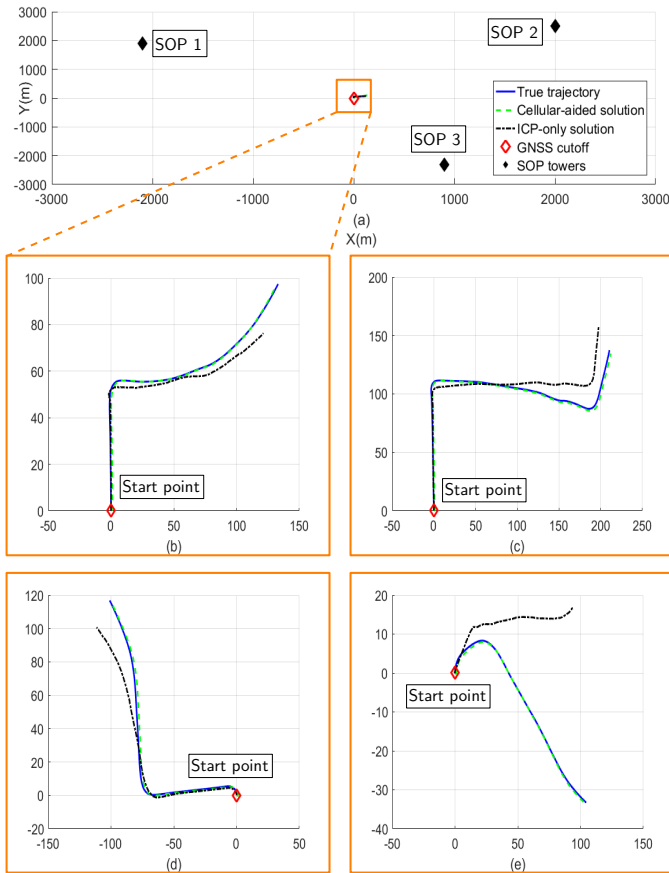


Fig. 8. Comparison of the simulation results with and without cellular aiding. (a) The simulation environment. The trajectory traversed by the vehicle is illustrated along with the position of 3 cellular towers. (b)–(e) Four different scenarios from the KITTI data set with simulated cellular pseudoranges. In each scenario, the ground truth and the ICP-only and the cellular-aided navigation solutions are depicted. As can be seen, the proposed approach outperforms the ICP-only framework.

In order to evaluate the impact of the number of cellular towers on the navigation performance, the first data set (Test 1)

TABLE II
VEHICLE'S POSITION RMSE ESTIMATION ERROR WITH THE ICP-ONLY LIDAR METHOD, CELLULAR-ONLY METHOD, AND THE PROPOSED CELLULAR-AIDED LIDAR METHOD

Test	ICP-only RMSE (m)	Cellular-only RMSE (m)	Cellular-aided RMSE (m)	Ratio of the error to total driven distance %
Test 1	10.15	8.42	1.57	0.88%
Test 2	11.78	7.68	1.78	0.6%
Test 3	8.49	9.14	2.11	1.4%
Test 4	26.16	5.14	0.60	0.75%

was repeated for $N_s = 2, \dots, 5$. The resulting position-RMSE and maximum error are tabulated in Table III. Comparable results were observed with the other data sets.

TABLE III
VEHICLE'S POSITION RMSE AND MAX. POSITION ESTIMATION ERROR WITH THE PROPOSED CELLULAR-AIDED LIDAR FOR A VARYING NUMBER OF CELLULAR TOWERS N_s

Number of towers (N_s)	RMSE error (m)	Max. error (m)
2	2.98	5.69
3	1.57	3.58
4	1.27	3.01
5	1.25	3.12

Fig. 9 illustrates the position of cellular tower 5, the initial estimate and corresponding uncertainty before the mapping mode, the estimate and corresponding uncertainty at the end of the mapping mode, and the estimate and corresponding uncertainty at the end of the SLAM mode for the first data set (Test 1). Comparable results were observed for other towers and data sets.

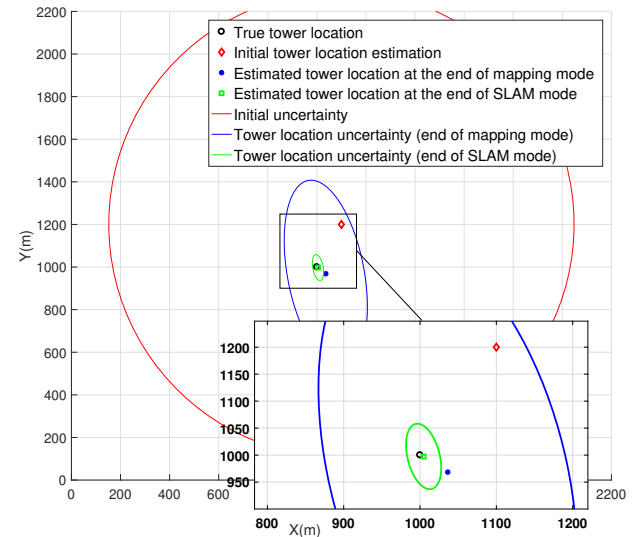


Fig. 9. The true position of cellular tower 5, the initial estimate and corresponding uncertainty before the mapping mode, the estimate and corresponding uncertainty at the end of the mapping mode, and the estimate and corresponding uncertainty at the end of the SLAM mode for the first data set (Test 1) are shown.

Table IV compares the computation time between the pro-

posed ICP and other approaches [8], [46]. It can be seen that the proposed neighbor searching method leads to faster convergence for registering the corresponding points of two successive lidar frames, while it achieves comparable accuracy.

TABLE IV
CONVERGENCE SPEED OF PROPOSED METHOD

Method	Computation time (s)	Iteration
Regular ICP	12.25	36
ICP in [32]	7.23	29
k-d tree	6.82	27
Ak-d tree [46]	0.94	28
ACK-d tree [8]	0.28	27
Proposed method	0.23	25

In contrast to existing lidar-based localization approaches where the accuracy of localization and mapping highly depends on the number of processed points in the point cloud, the proposed framework uses only 2.5% of the total points in each scan while continuously achieving lane-level accuracy. This results in a significant decrease in the computational burden, making the proposed framework suitable for real-time applications. In order to evaluate the impact of the reduction of the processed points in each scan on the navigation performance, the second data set (Test 2) was repeated by varying the number of processed points in the scanned point cloud. The position RMSE values are summarized in Table V. It can be seen that reducing the processed points in the point cloud does not have a considerable effect on the proposed cellular-aided solution accuracy. In contrast, reducing the processed points in the point cloud dramatically degrades the ICP-only solution accuracy.

TABLE V
VEHICLE'S POSITION RMSE WITH THE PROPOSED CELLULAR-AIDED LIDAR FOR A VARYING NUMBER OF PROCESSED POINTS IN EACH SCAN

% of the total points used in ICP	RMSE 2-D (m)	
	ICP-only solution	Cellular-aided solution
80%	2.54	0.91
50%	5.49	1.25
10%	9.27	1.42
2.5%	11.78	1.78

The following conclusion can be drawn from the presented simulation. First, the proposed framework yielded superior results to the ICP-only navigation solution. Second, the simulation results demonstrate that exploiting more towers yields a more accurate navigation solution, as expected. It is evident from Table III that increasing N_s from 2 to 3 yields the most improvement. Third, the proposed cellular-aided approach achieved significantly lower estimation error with fewer lidar scanned points than the ICP-only navigation solution. This is due to the fact that exploiting cellular SOPs can eliminate the drift arising from not using enough lidar scanned points in the ICP algorithm.

VI. EXPERIMENTAL RESULTS

A field test was conducted to validate the proposed framework. In this section, the experimental setup is first presented. Then, the different experiment scenarios are described and the corresponding results are shown.

A. Vehicle-Mounted Receiver Setup

A vehicle was equipped with a Velodyne HDL-64E lidar sensor whose x -axis points toward the front of the vehicle, z -axis points upward, and y -axis points to the right side of the car. The parameters of the lidar sensor are summarized in Table VI.

TABLE VI
VELODYNE HDL-64E LIDAR SENSOR

Parameter	Value
Measurement range	Up to 120 m
Vertical field of view	+2.0° to -24.9°
Horizontal field of view	360°
Rotation rate	5 – 20 Hz
Angular resolution	0.4°
Accuracy	±2.0 cm

The Velodyne scanner takes depth measurements continuously while rotating around its vertical axis. The frames returned by the lidar contain 90,000 3-D points. The proposed framework used 4,200 points of the point cloud (4.6% of the points). Over the course of the experiment, the ground-truth trajectory of the vehicle was obtained from its integrated GPS-IMU navigation system. The IMU returns six measurements (accelerations and rotational rates along the three orthogonal axes of the body frame B) at a rate of 100 Hz.

The car was also equipped with two cellular antennas to acquire and track signals from nearby cellular LTE towers. The LTE antennas used for the experiment were consumer-grade 800/1900 MHz cellular antennas. The signals were simultaneously down-mixed and synchronously sampled via a National Instruments (NI) dual-channel universal software radio peripheral (USRP)-2954R, driven by a GPS-disciplined oscillator (GSPDO). The clock bias and drift process noise power spectral densities of the receiver were set to be 1.3×10^{-22} s and 7.89×10^{-25} 1/s respectively, according to oven-controlled crystal oscillators (OCXO) used in (USRP)-2954R. The measurement noise covariance was set to be $10 m^2$, which were obtained empirically. The receiver was tuned to a carrier frequency of 1955 MHz, which is a channel allocated for U.S. cellular provider AT&T. Samples of the received signals were stored for off-line post-processing. The software-defined receiver (SDR) developed in [47] was used to produce LTE pseudoranges. For this field experiment, it was known to the receiver that the received signals pertain to cellular LTE base stations (also known as eNodeBs). If the signal structure is unknown, several SOP SDR modules (e.g., cellular code-division multiple access (CDMA), FM, etc.) may be run in parallel until the received signal is recognized, acquired, tracked, and data association between the produced pseudorange and the

corresponding SOP transmitter is performed. Fig. 10 illustrates the experimental hardware setup and traversed trajectory.

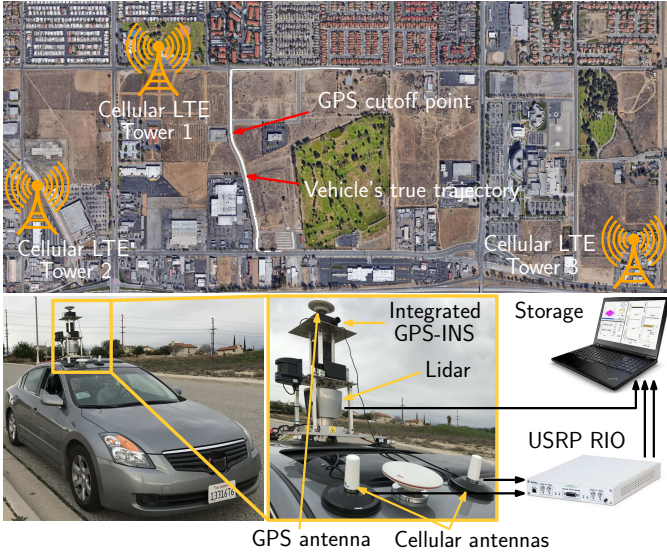


Fig. 10. A car was equipped with a lidar sensor, an integrated GPS-IMU navigation system, cellular antennas, and a USRP. The car traversed a suburban area collecting GPS, lidar, IMU measurements, and cellular LTE signals from three eNodeBs.

B. Scenario Description

The experiment considered the following scenario. A car that has access GPS starts driving in a straight segment heading up to a turning point. At about 200 m before the turning point, GPS signals become unavailable and remain so until the car travels 300 m after the turning point. The experiment scenario is illustrated in Fig. 11. At the starting point, the position and orientation of the vehicle are directly observable from the integrated GPS-IMU navigation system. The vehicle's North and East coordinates are shown in the first plot of Fig. 11, and the down component is shown in the second plot as a function of time. The vehicle starts by moving in the West direction. After 200 m, it makes a right turn heading North. After another 200 m, the vehicle-mounted cellular receiver starts producing pseudoranges to three unknown LTE eNodeBs (square-shaped segment in Fig. 11, which indicates the beginning of the mapping mode). The car keeps moving for 200 m then reaches the turning point where GPS becomes unavailable, leaving only cellular measurements to correct the lidar errors.

When the vehicle reaches the narrow turning point (the critical point in Fig. 11), it heads in the East direction. The segment in which GPS was unavailable is indicated by the green diamond-shaped marker in Fig. 11. This amounts to 40 s of GPS unavailability.

This experimental test was conducted in a suburban area in Riverside, California, USA where GPS signals were available along the entire trajectory to provide ground truth. However, the navigation solution obtained from the GPS receiver is discarded to emulate a GPS cutoff period during the experiment (shown as the dark green segment of the trajectory in Fig. 11). It is worth mentioning that in the experiment area, the cellular

towers were obstructed and far from the vehicle (more than 1.7 km), and large portion of the vehicle's trajectory had no clear LOS to the cellular towers.

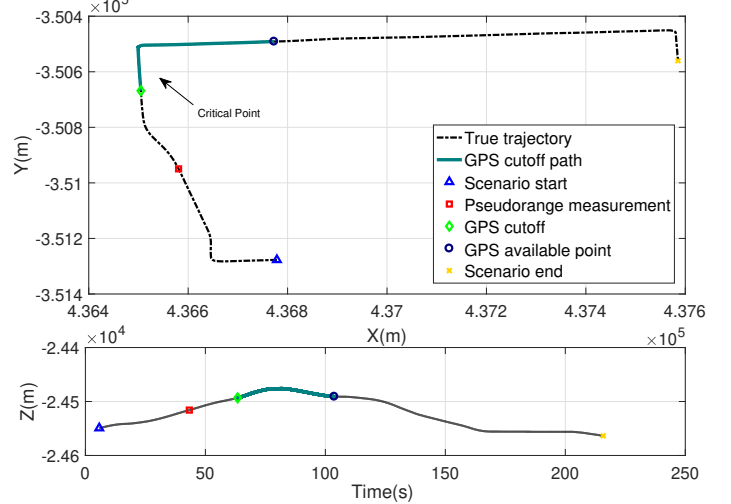


Fig. 11. Illustration of the experiment scenario. Top: Vehicle trajectory in x-y plane. Bottom: Vehicle trajectory in z axis. The black dashed line indicates the entire traversed trajectory. A wide green line indicates the part of the trajectory where GPS signals were unavailable. The location where the first cellular pseudorange is produced, the location where GPS signals become unavailable, and the location where the vehicle get access to GPS again are also indicated on the figure.

C. Navigation Results

Experimental results are presented for two estimation frameworks: (1) the cellular-aided solution described in this paper (plotted in Fig. 12(a)) and (2) the ICP-only solution (plotted in Fig. 12(b)).

The 3-D and 2-D vehicle position RMSEs of the cellular-aided navigation solution during GPS unavailability were 4.07 and 1.5 m, respectively. In contrast, when using ICP-only (Fig. 12(b)), the 3-D and 2-D RMSEs increased to 9.02 and 4.7 m, respectively. The mean and maximum errors for both 2-D and 3-D estimates are tabulated in Table VII. The maximum receiver position error using ICP-only was found to be 10.03 m for the 2-D estimate, whereas the maximum error using cellular aiding was 2.1 m.

TABLE VII
RECEIVER POSITION ESTIMATION ERRORS DURING GPS UNAVAILABILITY

Error (m)	ICP-only solution	Cellular-aided solution	Improvement	Ratio of the error to total driven distance %
RMSE 3-D	9.02	4.07	55.52%	1.3%
RMSE 2-D	4.73	1.50	68.08%	0.5%
Mean 3-D	10.7	4.23	62.61%	1.4%
Mean 2-D	8.16	1.26	85.18%	0.4%
Max. 3-D	15.14	5.07	66.97%	1.6%
Max. 2-D	10.03	2.10	80.00%	0.7%

It can be seen from Table VII that the proposed method significantly reduced the position error and achieved a 2-D mean position error of 1.26 m, which is within the lane-level

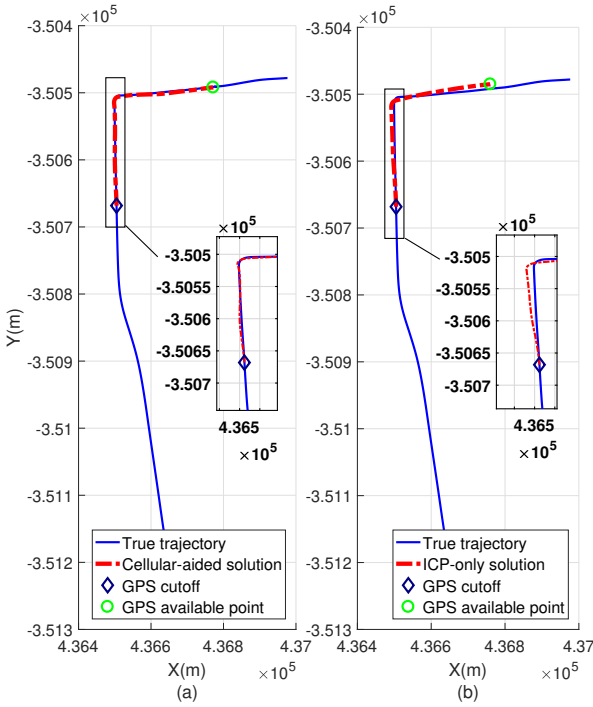


Fig. 12. Experimental results showing the true vehicle 2-D trajectory and the estimated vehicle trajectory: (a) With the proposed cellular-aided framework. (b) With the ICP-only framework.

[48]–[50]. It is worth noting that other work in the published literature achieved a comparable accuracy by fusing lidar with other sensors (e.g., vision [51], DGPS [52], and IMU [53]). However, the main motivation of the proposed framework is that in the absence of an aiding source to lidar, lidar odometry errors will accumulate. This paper proposes an approach to aid lidar with cellular signals of opportunity in the environment without the need to couple lidar with sensors or GNSS signals.

For a comparative analysis, the results achieved by the proposed framework is compared to the results achieved by the lidar odometry and mapping (LOAM) framework presented in [45]. LOAM achieved an accuracy of 0.9% over a distance of 58 m, while the accuracy obtained by the proposed cellular-aided framework was 0.4% over a distance of 300 m. It is worth noting that only three cellular towers were exploited in this experiment. As is shown in simulation result section, the RMSE reduction in cellular aiding will be even more significant when more towers are included. Moreover, note that the 2-D solution is more precise than the 3-D solution. This is due to the poor vertical dilution of precision inherent to terrestrial towers and minimal diversity in the towers' vertical positions.

The elements of the position and orientation vectors of the receiver during GPS unavailability are illustrated in Fig. 13. In this figure, the true trajectory and ICP-only and cellular-aided solutions are plotted. Fig. 13 (a) and (b) correspond to the x and y coordinates of the receiver, respectively. The blue line represents the true trajectory and the red line and the black line represent the cellular-aided and ICP-only solutions, respectively. Fig. 13 (c) and (d) correspond to the yaw and roll elements of the vehicle's orientation. The following may be

concluded from these plots. First, without aiding, a significant error is observed in both the position and orientation estimate of the vehicle when GPS signals are unavailable. With cellular aiding, these errors are reduced significantly. Second, the proposed approach is robust in areas with limited LOS to cellular towers. Third, experimental results show that using pseudoranges from 3 towers is sufficient to achieve lane-level 2-D position accuracy.

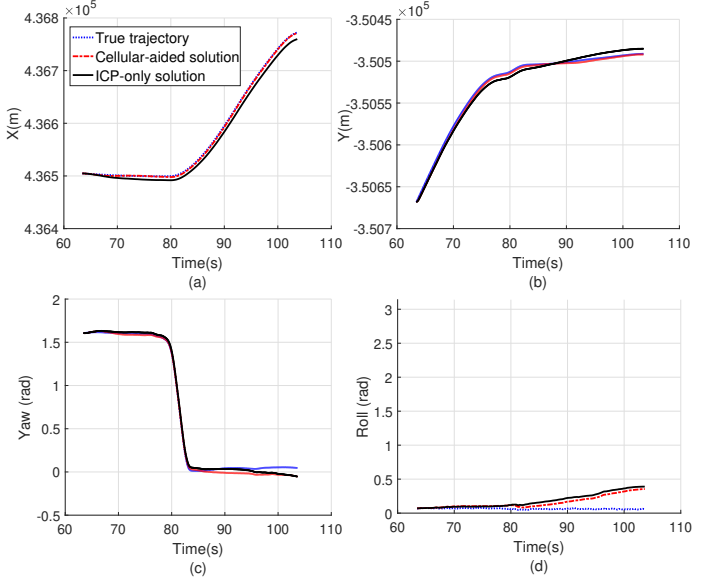


Fig. 13. (a)-(b) Vehicle horizontal position elements x and y . (c)-(d) Yaw and roll elements of the vehicle's orientation in radians. The blue dotted line represents the true trajectory, while the dashed red line and the solid black line represent the proposed cellular-aided and ICP-only solutions, respectively.

D. Cellular State Estimation Results

Fig. 14 illustrates the initial uncertainty in the EKF for the tower positions as the vehicle enters the mapping mode. In this figure, the vehicle has access to GPS signals, and the mapping mode framework presented in Subsection IV-C is employed to estimate the transmitters' states. The initial cellular position estimates were initialized using a symmetric array of cellular towers, leveraging the known structure of cellular networks. As shown in Fig. 14, the endpoints of an equilateral triangle were used as the initial cellular towers position estimates in this experimental test. The initial uncertainty in the towers' positions is set to 1 km. This uncertainty is large enough, based on the experimental records captured from Google Earth. The clock bias and drift of each transmitter were also initialized according to the approach presented in [54], in which the state estimate in the EKF was initialized according to

$$\hat{\mathbf{x}}_c(0| - 1) \sim \mathcal{N}[\mathbf{x}_c(0), \mathbf{P}_c(0| - 1)],$$

where $\mathbf{x}_c(0) = [c\Delta\delta t_n(0), c\Delta\dot{\delta}t_n(0)]^\top$ and $c\Delta\delta t_n(0) \triangleq d_r(0) - z_{s_n}(0)$ and $c\Delta\dot{\delta}t_n(0) \triangleq (\Delta\delta t_n(1) - \Delta\delta t_n(0))/T$, where $d_r(0)$ is the distance between the receiver and the transmitters, calculated using the last coordinate obtained from GNSS signals, and $\mathbf{P}_c(0| - 1) \equiv (10^4) \cdot \text{diag}[3, 0.3]$.

Fig. 15 illustrates the towers' position estimates and the associated uncertainties at the moment GPS is cutoff. After

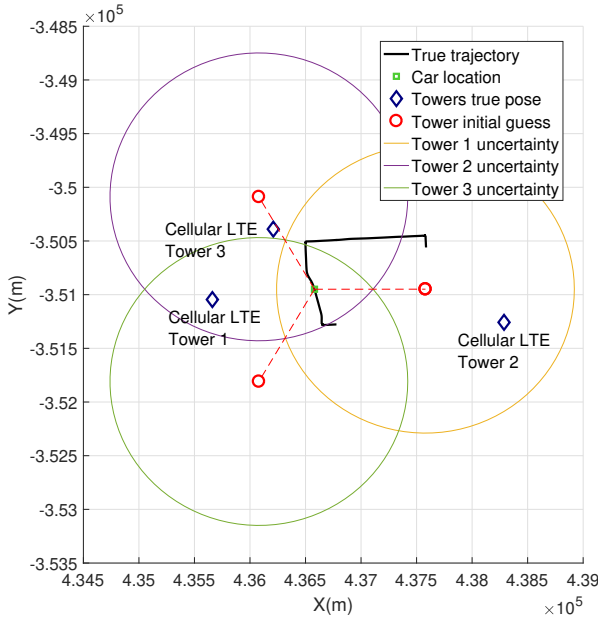


Fig. 14. The initial towers' position estimates were initialized using a symmetric array of towers, leveraging the known structure of cellular networks. The endpoints of an equilateral triangle were used as the initial towers' position estimates in this experimental test.

this point, the SLAM mode framework is employed to simultaneously map the cellular transmitters and localize the vehicle. The solid green line represents the path during which GPS was available and the vehicle was in mapping mode.

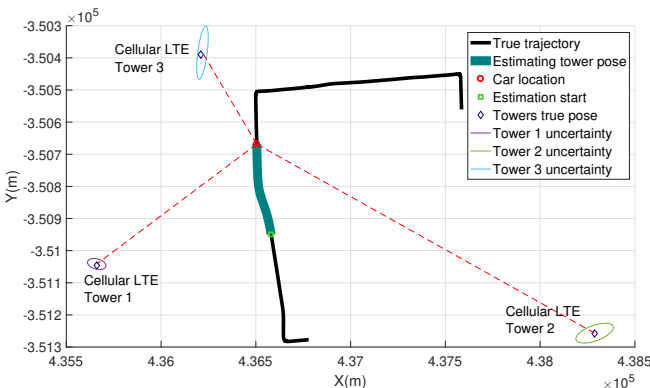


Fig. 15. The moment at which GPS is cutoff. After this point, the vehicle enters the SLAM mode where it estimates the cellular transmitters' states and simultaneously localizes itself.

The transmitters position estimation errors at key points on the total trajectory are tabulated in Table VIII. It can be seen that, the initial error for the third cellular tower was 476.31 m. By the end of the mapping mode, this error was reduced to 10.57 m. By the end of the SLAM mode, this error was reduced to below 5 m.

Fig. 16 shows the position estimation error trajectories and corresponding $\pm 2\sigma$ for the three cellular towers. Fig. 16(a)–(c) illustrate the x position error for all cellular transmitters over the entire trajectory. The dashed black line represents the moment GPS signals became unavailable. The dashed green line represents the moment GPS signals became available again.

TABLE VIII
CELLULAR TOWER POSITION ESTIMATION ERRORS

Point on trajectory	Tower 1 error (m)	Tower 2 error (m)	Tower 3 error (m)
Start of mapping mode	576.39	804.97	476.31
GPS cutoff	12.23	9.95	10.56
GPS available again	3.97	1.79	3.69

Figs. 16(d)–(f) illustrate the y position error for all towers. The following may be concluded from these plots. First, in both the mapping mode and SLAM mode, the estimation error uncertainties converged and remained bounded, as expected. Second, it can be seen from Figs. 16(d)–(f) that the estimator's transient phase is less than 5 seconds.

Next, the performance of the proposed framework is compared with the cellular-only navigation framework presented in [55]. In [55], only cellular transmitters 1 and 2 were used. Therefore, the experimental results presented in this paper were processed again using only two cellular transmitters. Table IX compares the navigation performance obtained by the proposed algorithm versus that of the cellular-only navigation framework presented in [55]. It can be seen that incorporating the proposed cellular+lidar algorithm reduced the position RMSE by 79% from the RMSE obtained by a cellular-only navigation solution.

TABLE IX
COMPARISON BETWEEN THE PROPOSED FRAMEWORK AND THE CELLULAR-ONLY NAVIGATION SOLUTION

Performance measure	Cellular-only navigation solution	Proposed approach
RMSE 2-D	9.32 m	1.91 m
Standard deviation 2-D	4.36 m	1.21 m
Max. 2-D	33.47 m	6.73 m

VII. CONCLUSION

In this paper, a framework for vehicular simultaneous localization and mapping is developed that uses lidar data and pseudoranges extracted from ambient cellular LTE towers. The framework achieves lane-level localization without GNSS signals. In this framework, an ICP algorithm was employed to extract odometry measurements from successive lidar scans. A robust and computationally efficient feature extraction method was proposed to detect edge lines and feature points from the lidar's point cloud. Then, a point registration technique was developed using a maximum likelihood approach. This allows the estimation of the covariance of the odometry error, which is needed for the EKF propagation step. The proposed approach consists of (1) mapping mode in when GNSS signals are available and (2) SLAM mode when GNSS signals become unavailable. The cellular transmitters' states, namely position and clock bias and clock drift, are continuously estimated in both modes. Simulation and experimental results validate the accuracy of the proposed framework. Experiments results involving with a Velodyne HDL-64E lidar sensor and cellular antennas to acquire and track signals from nearby LTE

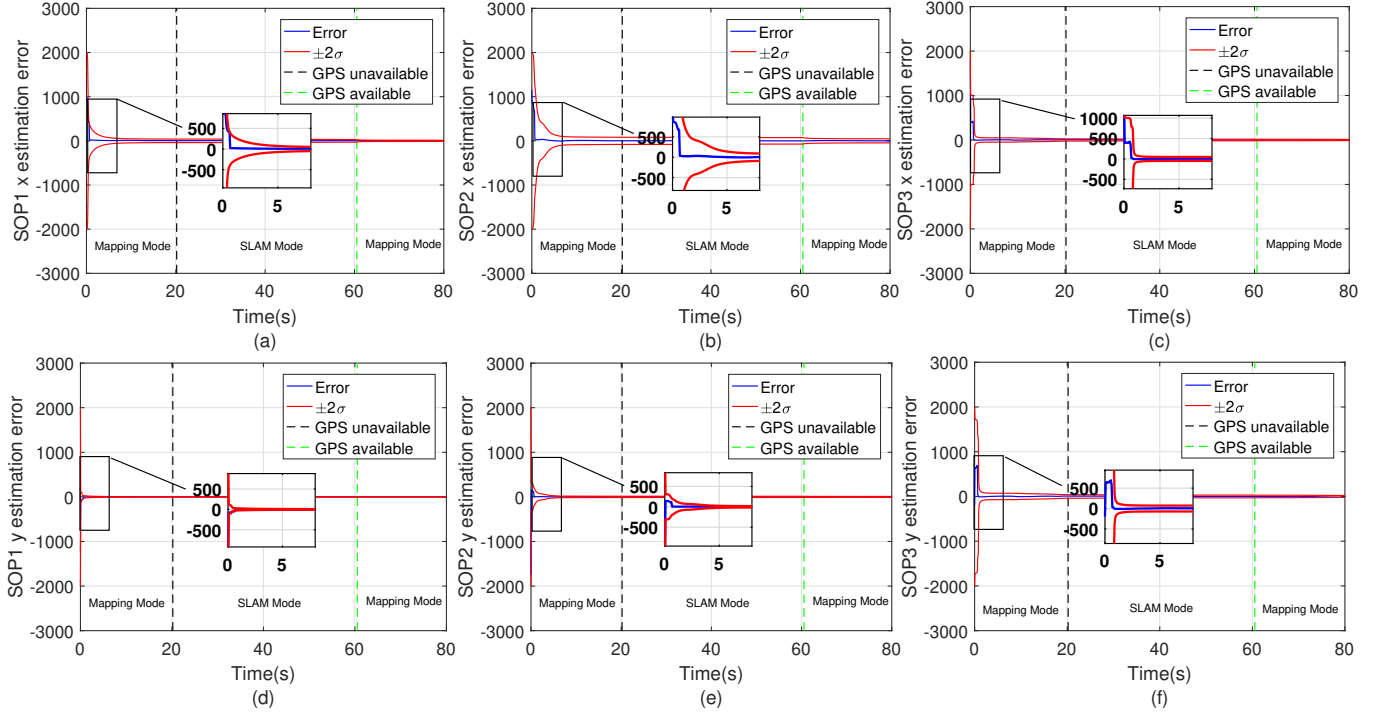


Fig. 16. The resulting position estimation errors and corresponding $\pm 2\sigma$ bounds for the 3 cellular towers. The states of the towers are continuously estimated during both the mapping and SLAM modes. (a)–(c) Estimation error in the x -direction for towers 1, 2, and 3. (d)–(f) Estimation error in the y -direction for towers 1, 2, and 3.

transmitters were presented. The proposed framework was compared with an ICP-only solution over a total traversed trajectory of 1 km. Results show that the proposed framework improve the navigation solution of the ICP-only framework by more than 60%. The 2-D RMSE of the ICP-only solution was 40 m, whereas the RMSE of the cellular-aided solution was below 1.5 m.

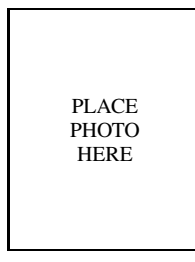
ACKNOWLEDGMENT

The authors would like to thank Alex Vu, Sonya Ragothaman, Joshua Morales, Luting Yang, and Kimia Shamaei for their help with the data collection.

REFERENCES

- [1] A. Hata and D. Wolf, "Feature detection for vehicle localization in urban environments using a multilayer Lidar," *IEEE Transactions on Intelligent Transportation Systems*, vol. 17, no. 2, pp. 420–429, February 2016.
- [2] H. Luo, C. Wang, C. Wen, Z. Cai, Z. Chen, H. Wang, Y. Yu, and J. Li, "Patch-based semantic labeling of road scene using colorized mobile Lidar point clouds," *IEEE Transactions on Intelligent Transportation Systems*, vol. 17, no. 5, pp. 1286–1297, May 2016.
- [3] M. Tan, B. Wang, Z. Wu, J. Wang, and G. Pan, "Weakly supervised metric learning for traffic sign recognition in a Lidar-equipped vehicle," *IEEE Transactions on Intelligent Transportation Systems*, vol. 17, no. 5, pp. 1415–1427, May 2016.
- [4] B. Paden, M. Cap, S. Yong, D. Yershov, and E. Frazzoli, "A survey of motion planning and control techniques for self-driving urban vehicles," *IEEE Transactions on Intelligent Vehicles*, vol. 1, no. 1, pp. 33–55, March 2016.
- [5] L. Li, M. Yang, L. Guo, C. Wang, and B. Wang, "Hierarchical neighborhood based precise localization for intelligent vehicles in urban environments," *IEEE Transactions on Intelligent Vehicles*, vol. 1, no. 3, pp. 220–229, September 2016.
- [6] K. Takeyama, T. Machida, Y. Kojima, and N. Kubo, "Improvement of dead reckoning in urban areas through integration of low-cost multisensors," *IEEE Transactions on Intelligent Vehicles*, vol. 2, no. 4, pp. 278–287, December 2017.
- [7] H. Fang, M. Yang, and R. Yang, "Ground texture matching based global localization for intelligent vehicles in urban environment," in *Proceedings of IEEE Intelligent Vehicles Symposium*, June 2007, pp. 105–110.
- [8] W. Choi, Y. Kim, S. Oh, and J. Lee, "Fast iterative closest point framework for 3D LIDAR data in intelligent vehicle," in *Proceedings of IEEE Intelligent Vehicles Symposium*, June 2012, pp. 1029–1034.
- [9] T. Gee, J. James, W. V. D. Mark, P. Delmas, and G. Gimel'farb, "Lidar guided stereo simultaneous localization and mapping (SLAM) for UAV outdoor 3-D scene reconstruction," in *International Conference on Image and Vision Computing*, November 2016, pp. 1–6.
- [10] J. Zhang and S. Singh, "Visual-lidar odometry and mapping: low-drift, robust, and fast," in *Proceedings of IEEE International Conference on Robotics and Automation*, May 2015, pp. 2174–2181.
- [11] J. Rohde, B. Volz, H. Mielenz, and J. Zollner, "Precise vehicle localization in dense urban environments," in *Proceedings of IEEE International Conference on Intelligent Transportation Systems*, November 2016, pp. 853–858.
- [12] G. Grisetti, S. Grzonka, C. Stachniss, P. Pfaff, and W. Burgard, "Efficient estimation of accurate maximum likelihood maps in 3D," in *Proceedings of International Conference on Intelligent Robots and Systems*, November 2007, pp. 3472–3478.
- [13] A. Nuchter, J. Elseberg, P. Schneider, and D. Paulus, "Linearization of rotations for globally consistent n-scan matching," in *Proceedings of IEEE International Conference on Robotics and Automation*, May 2010, pp. 7888–7894.
- [14] H. Song, W. Choi, and H. Kim, "Robust vision-based relative-localization approach using an RGB-depth camera and LiDAR sensor fusion," *IEEE Transactions on Industrial Electronics*, vol. 63, no. 6, pp. 3725–3736, June 2016.
- [15] J. Zhang, M. Kaess, and S. Singh, "Real-time depth enhanced monocular odometry," in *Proceedings of IEEE/RSJ International Conference on Intelligent Robots and Systems*, September 2014, pp. 4973–4980.
- [16] S. Zhao and J. Farrell, "2D LIDAR aided INS for vehicle positioning in urban environments," in *Proceedings of IEEE International Conference on Control Applications*, August 2013, pp. 376–381.

- [17] A. Garcia-Moreno and J. Gonzalez-Barbosa, "GPS precision time stamping for the HDL-64E Lidar sensor and data fusion," in *Proceedings of IEEE Electronics, Robotics and Automotive Mechanics Conference*, November 2012, pp. 48–53.
- [18] A. Peker and T. Acarman, "VANET-assisted cooperative vehicle mutual positioning: Feasibility study," *IEICE Transactions on Fundamentals of Electronics, Communications and Computer Sciences*, vol. E100.A, no. 2, pp. 448–456, 2017.
- [19] L. Merry, R. Faragher, and S. Schedin, "Comparison of opportunistic signals for localisation," in *Proceedings of IFAC Symposium on Intelligent Autonomous Vehicles*, September 2010, pp. 109–114.
- [20] K. Pesyna, Z. Kassas, J. Bhatti, and T. Humphreys, "Tightly-coupled opportunistic navigation for deep urban and indoor positioning," in *Proceedings of ION GNSS Conference*, September 2011, pp. 3605–3617.
- [21] Z. Kassas, "Collaborative opportunistic navigation," *IEEE Aerospace and Electronic Systems Magazine*, vol. 28, no. 6, pp. 38–41, 2013.
- [22] C. Yang, T. Nguyen, and E. Blasch, "Mobile positioning via fusion of mixed signals of opportunity," *IEEE Aerospace and Electronic Systems Magazine*, vol. 29, no. 4, pp. 34–46, April 2014.
- [23] Z. Kassas, J. Khalife, K. Shamaei, and J. Morales, "I hear, therefore I know where I am: Compensating for GNSS limitations with cellular signals," *IEEE Signal Processing Magazine*, pp. 111–124, September 2017.
- [24] J. Khalife, K. Shamaei, and Z. Kassas, "A software-defined receiver architecture for cellular CDMA-based navigation," in *Proceedings of IEEE/ION Position, Location, and Navigation Symposium*, April 2016, pp. 816–826.
- [25] K. Shamaei, J. Khalife, and Z. Kassas, "Exploiting LTE signals for navigation: Theory to implementation," *IEEE Transactions on Wireless Communications*, vol. 17, no. 4, pp. 2173–2189, April 2018.
- [26] J. Morales, P. Roysdon, and Z. Kassas, "Signals of opportunity aided inertial navigation," in *Proceedings of ION GNSS Conference*, September 2016, pp. 1492–1501.
- [27] Z. Kassas, J. Morales, K. Shamaei, and J. Khalife, "LTE steers UAV," *GPS World Magazine*, vol. 28, no. 4, pp. 18–25, April 2017.
- [28] J. Morales and Z. Kassas, "Distributed signals of opportunity aided inertial navigation with intermittent communication," in *Proceedings of ION GNSS Conference*, September 2017, pp. 2519–2530.
- [29] J. Morales, J. Khalife, and Z. Kassas, "GNSS vertical dilution of precision reduction using terrestrial signals of opportunity," in *Proceedings of ION International Technical Meeting Conference*, January 2016, pp. 664–669.
- [30] J. Morales, J. Khalife, and Z. Kassas, "Opportunity for accuracy," *GPS World Magazine*, vol. 27, no. 3, pp. 22–29, March 2016.
- [31] K. Shamaei and Z. Kassas, "LTE receiver design and multipath analysis for navigation in urban environments," *NAVIGATION, Journal of the Institute of Navigation*, 2017, submitted.
- [32] J. Khalife, S. Ragothaman, and Z. Kassas, "Pose estimation with lidar odometry and cellular pseudorange," in *Proceedings of IEEE Intelligent Vehicles Symposium*, June 2017, pp. 1722–1727.
- [33] Z. Kassas, V. Ghadiok, and T. Humphreys, "Adaptive estimation of signals of opportunity," in *Proceedings of ION GNSS Conference*, September 2014, pp. 1679–1689.
- [34] G. Bresson, Z. Alsayed, L. Yu, and S. Glaser, "Simultaneous localization and mapping: A survey of current trends in autonomous driving," *IEEE Transactions on Intelligent Vehicles*, vol. 2, no. 3, pp. 194–220, September 2017.
- [35] A. Geiger, P. Lenz, and R. Urtasun, "Are we ready for autonomous driving? The KITTI vision benchmark suite," in *Proceedings of Conference on Computer Vision and Pattern Recognition*, June 2012, pp. 3354–3361.
- [36] Z. Kassas and T. Humphreys, "Observability analysis of collaborative opportunistic navigation with pseudorange measurements," *IEEE Transactions on Intelligent Transportation Systems*, vol. 15, no. 1, pp. 260–273, February 2014.
- [37] A. Thompson, J. Moran, and G. Swenson, *Interferometry and Synthesis in Radio Astronomy*, 2nd ed. John Wiley & Sons, 2001.
- [38] P. Besl and N. McKay, "A method for registration of 3-D shapes," *IEEE Transactions on Pattern Analysis and Machine Intelligence*, vol. 14, no. 2, pp. 239–256, February 1992.
- [39] S. Rusinkiewicz and M. Levoy, "Efficient variants of the icp algorithm," in *Proceedings of 3-D Digital Imaging and Modeling*, May 2001, pp. 145–152.
- [40] J. Dong, Z. Cai, and S. Du, "Improvement of affine iterative closest point algorithm for partial registration," *IET Computer Vision*, vol. 11, no. 2, pp. 135–144, March 2017.
- [41] W. Fu, M. Johnston, and M. Zhang, "Low-level feature extraction for edge detection using genetic programming," *IEEE Transactions on Cybernetics*, vol. 44, no. 8, pp. 1459–1472, August 2014.
- [42] A. Nascimento, M. Horta, A. Frery, and R. Cintra, "Comparing edge detection methods based on stochastic entropies and distances for PolSAR imagery," *IEEE Journal of Selected Topics in Applied Earth Observations and Remote Sensing*, vol. 7, no. 2, pp. 648–663, February 2014.
- [43] C. Weber, S. Hahmann, and H. Hagen, "Sharp feature detection in point clouds," in *Proceedings of Shape Modeling International Conference*, June 2010, pp. 175–186.
- [44] KITTI vision benchmark suite. [Online]. Available: <http://www.cvlibs.net/datasets/kitti/>
- [45] J. Zhang and S. Singh, "LOAM: Lidar odometry and mapping in real-time," in *Proceedings of Robotics: Science and Systems Conference*, July 2014, pp. 949–951.
- [46] M. Greenspan and M. Yurick, "Approximate k-d tree search for efficient ICP," in *Proceedings of International Conference on 3-D Digital Imaging and Modeling*, October 2003, pp. 442–448.
- [47] K. Shamaei, J. Khalife, and Z. Kassas, "Performance characterization of positioning in LTE systems," in *Proceedings of ION GNSS Conference*, September 2016, pp. 2262–2270.
- [48] A. Vu, A. Ramanandan, A. Chen, J. Farrell, and M. Barth, "Real-time computer vision/DGPS-aided inertial navigation system for lane-level vehicle navigation," *IEEE Transactions on Intelligent Transportation Systems*, vol. 13, no. 2, pp. 899–913, June 2012.
- [49] D. Cui, J. Xue, and N. Zheng, "Real-time global localization of robotic cars in lane level via lane marking detection and shape registration," *IEEE Transactions on Intelligent Transportation Systems*, vol. 17, no. 4, pp. 1039–1050, April 2016.
- [50] Y. Gu, L. Hsu, and S. Kamijo, "GNSS/Onboard inertial sensor integration with the aid of 3-D building map for lane-level vehicle self-localization in urban canyon," *IEEE Transactions on Vehicular Technology*, vol. 65, no. 6, pp. 4274–4287, June 2016.
- [51] A. Vu and J. Farrell, "Feature mapping and state estimation for highly automated vehicles," *Journal of Control and Decision*, vol. 2, no. 1, pp. 1–25, February 2015.
- [52] J. Kim, J. Kim, J. Kim, T. Jung, Y. Park, Y. Ko, and S. Jung, "Experimental studies of autonomous driving of a vehicle on the road using LIDAR and DGPS," in *Proceedings of International Symposium on Control, Automation and Systems*, October 2015, pp. 1366–1369.
- [53] C. Peng, Y. Wang, and C. Chen, "LIDAR based scan matching for indoor localization," in *Proceedings of International Symposium on System Integration*, December 2017, pp. 139–144.
- [54] J. Morales and Z. Kassas, "Optimal collaborative mapping of terrestrial transmitters: receiver placement and performance characterization," *IEEE Transactions on Aerospace and Electronic Systems*, vol. 54, no. 2, pp. 992–1007, April 2018.
- [55] K. Shamaei, J. Khalife, and Z. Kassas, "Comparative results for positioning with secondary synchronization signal versus cell specific reference signal in LTE systems," in *Proceedings of ION International Technical Meeting Conference*, January 2017, pp. 1256–1268.



real-time systems.

Mahdi Maaref Mahdi Maaref received the B.E degree in Electrical Engineering from the University of Tehran in 2008 and M.Sc. degree in Electrical Engineering-Power System at the same University in 2011 and Ph.D. Degree in Electrical Engineering at Shahid Beheshti University, Tehran, Iran in 2016. He was a visiting research collaborator at the University of Alberta, Edmonton, Canada in 2016. Currently, he is a postdoctoral research fellow at University of California, Riverside. His main interest is on opportunistic perception, distributed estimation and

PLACE
PHOTO
HERE

Joe Khalife (S'2015) is a Ph.D. student at the University of California, Riverside. He received a B.E. in electrical engineering and an M.S. in computer engineering from the Lebanese American University (LAU). From 2012 to 2015, he was a research assistant at LAU. His research interests include opportunistic navigation, autonomous vehicles, and software-defined radio.

PLACE
PHOTO
HERE

Zaher (Zak) M. Kassas (S'98-M'08-SM'011) is an assistant professor at the University of California, Riverside and director of the autonomous systems perception, intelligence, and navigation (ASPIN) laboratory. He received a B.E. in Electrical Engineering from the Lebanese American University, an M.S. in Electrical and Computer Engineering from The Ohio State University, and an M.S.E. in Aerospace Engineering and a Ph.D. in Electrical and Computer Engineering from The University of Texas at Austin. In 2018, he received the NSF Faculty Early Career

Development Program (CAREER) award. His research interests include cyber-physical systems, estimation theory, navigation systems, autonomous vehicles, and intelligent transportation systems.